THE ASTROPHYSICAL JOURNAL, 430:511–532, 1994 August 1

DYNAMICS AND X-RAY EMISSION OF A GALACTIC SUPERWIND INTERACTING WITH DISK AND HALO GAS

ANATOLY A. SUCHKOV,[1] DINSHAW S. BALSARA,[2] TIMOTHY M. HECKMAN,[1,2] AND CLAUS LEITHERER[1]
Received 1993 September 17; accepted 1994 January 28

ABSTRACT

There is a general agreement that the conspicuous extranuclear X-ray, optical-line, and radio-continuum emission of starbursts is associated with powerful galactic superwinds blowing from their centers. However, despite the significant advances in observational studies of superwinds, there is no consensus on the nature of the emitting material and even on the emission mechanisms themselves. This is to a great extent a consequence of a poor understanding of dynamical processes in the starburst superwind regions. To address this issue, we have conducted two-dimensional hydrodynamical simulations of galactic superwinds. While previous similar studies have used a single (disk) component to represent the ISM of the starburst galaxy, we analyze the interaction of the wind with a *two-component disk-halo ambient interstellar medium* and argue that this two-component representation is crucial for adequate modeling of starbursts.

The emphasis of this study is on the geometry and structure of the wind region and the X-ray emission arising in the wind material and the shocked gas in the disk and the halo of the galaxy. The simulation results have shown that a clear-cut bipolar wind can easily develop under a range of very different conditions. On the other hand, a complex "filamentary" structure associated with the entrained dense disk material is found to arise within the hot bubble blown out by the wind. The flow pattern within the bubble is dominated equally by the central biconic outflow and a system of whirling motions related to the origin and development of the "filaments." The filament parameters make them a good candidate for optical–emission-line filamentary gas observed in starburst halos. We find that *the history of mass and energy deposition in the starburst region of the galaxy is crucial for wind dynamics.* A "mild" early wind, which arises as a result of the cumulative effect of stellar winds from massive stars, produces a bipolar vertical cavity in the disk and halo gas without strongly affecting the gaseous disk, thus creating conditions for virtually free vertical escape of the hot gas at the later, much more violent supernova-dominated phases of the starburst.

We calculate the luminosity, mass, and effective temperature of the X-ray emitting gas in the "soft" (0.1–0.7 keV, 0.7–2.2 keV, and 0.1–2.2 keV) and "hard" (1.6–8.3 keV) energy bands and estimate the contribution of different gaseous components to the X-ray flux in these bands. Analysis of these parameters enables us to make conclusions regarding the nature of the X-ray-emitting material. We have inferred that *the bulk of the soft thermal X-ray emission from starbursts arises in the wind-shocked material of the disk and halo gas rather than in the wind material itself.* This enables us to predict that *the integrated soft X-ray spectra of starbursts need not show an overabundance of heavy elements* which are believed to be produced copiously in the centers of starbursts. Unlike soft X-ray emission, the hard component of thermal X-ray emission is found to originate in the wind material ejected from the starburst region. However, the derived ratio of hard-to-soft X-ray luminosities is too small compared to that observed in starbursts. We conclude therefore that *the observed hard X-ray emission of starbursts is probably not associated with the thermal emission of hot wind or ambient shocked gas.*

Typical temperatures of the bulk of the soft X-ray–emitting material in our very different models have been found to agree well with the ones estimated on the basis of the *ROSAT* data for the soft component of X-ray emission of nearby starbursts. We predict that *temperatures of the extranuclear soft X-ray–emitting gas in starburst galaxies with heavy element abundances near solar should be close to* $T_{Xs} = 2\text{–}5 \times 10^6$ K.

Subject headings: galaxies: ISM — galaxies: kinematics and dynamics — galaxies: starburst — galaxies: structure — X-rays: galaxies

1. INTRODUCTION

Strong galactic winds (superwinds) arising during the starburst phase of galaxies are believed to be responsible for the bulk of the starburst soft X-ray emission, radio emission, and optical line emission located outside the starburst itself (see, e.g., Heckman, Lehnert, & Armus 1993, hereafter HLA and references therein). No wonder that galactic superwinds have over the past few years been the focus of many observational studies in essentially all wavelength bands (see, e.g., HLA and references therein). In view of the large amount of activity in this field it is rather remarkable that there is a scarcity of efforts to model a plethora of superwind-related phenomena, both gas-dynamical and radiative, which are observed to occur in starbursts.

A number of important issues related to starbursts can be addressed through hydrodynamical simulations of galactic winds. One of them is that of the wind geometry, which is crucial for interpretation of the observed starburst emission and for inferences regarding the effects of galactic winds upon

[1] Space Telescope Science Insitute operated by AURA Inc., under contract with NASA, Baltimore, MD 21218, USA.
[2] Department of Physics and Asronomy, Johns Hopkins University, Baltimore, MD 21218.

star formation and galaxy evolution. The wind geometry appears to be intimately connected with the structure of the interstellar medium in the starbursts. Mathews & Doane (1992, hereafter MD) have pointed out that the prevailing concept of a galactic wind as a bipolar flow is due largely to theoretical studies in which winds are considered as arising in the plane-parallel gaseous atmosphere of a galactic disk with a vertical density gradient. An initial study of this kind (although not exactly for a plane-parallel atmosphere) was that of Tomisaka & Ikeuchi (1988, hereafter TI) who conducted hydrodynamical simulations of a bipolar galactic wind for a model of the starburst galaxy M82. Mathews & Doane questioned this model by arguing that the state of the actual gas component in galactic disks like that in M82 is different from the one envisioned by TI in the sense that the gaseous disks would offer much less resistance to the hot gas produced by supernovae than is required to channel the hot outflow along the galaxy minor axis.

A relevant point, also emphasized by MD, is that most of the hydrodynamical modeling of starbursts was restricted to initial, transient phases of galactic winds. They argued that as soon as the wind becomes "fully mature," it will lose memory of the initial geometry and become essentially spherically symmetric. Based on these arguments, MD developed a steady state wind model which ignores the effects of the galactic gaseous component on the wind at all.

The models of TI and MD offer dramatically different physics for the processes responsible for the most conspicuous manifestations of the galactic winds, namely, their extended X-ray emission and nonthermal radio emission. The former one explains the observed X-ray emission in M82 as the thermal emission of the hot wind. The X-ray luminosity predicted for the starburst after it has progressed for a few megayears after the onset of the wind has been found to be compatible with observational data if the conventional estimate for the supernova rate of 0.1 SN per year is adopted. But the MD model yields a value for the wind X-ray luminosity that is too low even at larger SN rates. Therefore MD have proposed another mechanism for the origin of X-ray emission. They speculated that there are thermally unstable regions in the galactic wind where cosmic ray electrons are reaccelerated to the extent that they become capable of producing the observed amount of X-rays via inverse Compton scattering of infrared photons generated in the starburst. MD have further argued that the radio surface brightness morphology in M82 is suggestive of dominating role of reaccelerated cosmic rays, and hypothesized that basically the same process of thermal instability is responsible for both the extended X-ray emission and nonthermal radio emission.

Although the paper of MD is an important step toward understanding starbursts, its major starting point, namely that the mature winds lose memory of the initial conditions, can hardly be accepted. Features of bipolarity are certainly present in the extended X-ray image of M82 (Fabbiano 1988) and NGC 3628 (Fabbiano, Heckman, & Keel 1990; Heckman & Fabbiano 1993). *ROSAT* data show that the same is true for NGC 253: the extension of the soft (0.1–0.5 keV) X-ray image of this galaxy along the minor axis is more than 70% larger than that along the major axis ($>26'$ and $\approx 15'$, respectively; Pietsch 1993). Another important piece of evidence in favor of a bipolar wind in M82 is provided by line-emitting clouds. Back in the 1960s, Burbidge, Burbidge, & Rubin (1964) inferred that the extended ionized gas in M82 outlines a biconic geometry with the apparent opening half-angle of $\approx 22°$. This conclusion has been substantiated by Heckman, Armus, & Miley (1990, hereafter HAM) on the basis of a detailed spectroscopy of the line-emitting clouds in M82 as well as in a few other starburst galaxies: NGC 253, NGC 4945, Arp 220, and NGC 3079. The primary cloud emission properties listed in HAM as typical for all of the mentioned galaxies have been successfully explained in a self-consistent way in a model of a bipolar outflow along a biconic surface, with rather small and nearly constant opening angle ($\theta = 60°$–$80°$ for NGC 253, M82, and NGC 4945). The data also suggest that the ionized clouds are confined to the outer surface of the cones, the interior of the cones being essentially hollow. This is to be expected for a biconic wind interacting with the ambient galactic gas. So, even a "mature" wind as that in M82 may still preserve strong features of a biconic geometry, which is indicative of a significant role for the ambient galactic gas not only in the early development of the wind but also in the current properties of "mature" starbursts. Another support for the latter conclusion can be found in a number of spectacular features observed in ultraluminous infrared galaxies, such as bright Hα arcs circumjacent Arp 220 (see Fig. 2 in Heckman, Armus, & Miley 1987). The two rather regular arcs extending tens-of-kiloparsecs above the central gas disk of this galaxy are suggestive of the circumgalactic gas swept out and compressed by the shock produced by the superwind.

There are three major factors which may have a strong impact on wind dynamics, and hence on the morphology and X-ray emission of the wind-blown superbubble. These are the time dependence of the deposition rates for mass and energy in the starburst, the mass and distribution of the ambient ISM, and the ISM clumpiness. The main idea of the paper of TI was that the observational manifestations of the starburst wind are determined by interaction of the wind with the ambient interstellar medium. The simulations conducted in that paper were made for a simplified model of the galaxy ISM which included a rotationally supported gaseous disk in which the angular speed was independent of the distance from the disk midplane. The vertical support of the disk was assumed to be provided by random motions of gas clouds rather than by thermal pressure. A simplified approach was adopted also in regard to the starburst event, which was modeled by deposition of mass and energy at a constant rate in the center of the galaxy. The main conclusions reached by TI were, first, that bipolar starburst winds can be produced by the combined effects of large mass and energy deposition from supernova explosions in the centers of starburst galaxies and that collimation of the resulting hot gas outflow by the galaxy gaseous disk occurs. Second, the wind material that is shocked as a result of interaction with the disk gas can account for the observed extended X-ray emission of the starbursts. These important conclusions called for examination of models which would more adequately reflect the actually much more complex situation in starbursts. There was also a desire to examine other implications of the wind-ambient ISM interaction. Thus Tomisaka & Bregman (1993) have extended TI's starburst model by adding to the dense, cold gas disk a corotating component of hot, low-density gas representing the halo ISM. The rotational velocity was specified to slowly decrease with increasing distance from the galactic midplane. As compared to TI, these authors found that allowing for the extended tenuous halo substantially increases the contribution of the shocked ambient gas to the total X-ray emission, so that most of the

emission comes from this gas. Also, alongside with calculating X-ray emission for the *Einstein Observatory* HRI band similar to TI, they calculated X-ray emission for a band which approximated the *Ginga* LAC band, so that they were able to make predictions regarding much harder thermal X-ray emission than that measured by *Einstein Observatory* and *ROSAT*.

In this paper we make the next step in modeling starburst winds by incorporating into our simulations the following new features:

1. A two-component structure for the ambient ISM, which includes kinematically and physically distinct disk and halo gas (rapidly rotating dense, cold disk, and nonrotating tenuous, hot halo).
2. The history of the starburst event, starting from initially "mild" deposition of mass and energy from stellar winds of massive stars through the violent, supernova-dominated phases of the starburst.
3. Separate treatment of three different gaseous species participating in the wind: the material of stellar winds and supernova ejecta, disk gas, and halo gas.
4. Calculation of thermal X-ray emission in three different energy bands, with two of them covering the "soft" and "hard" parts of the *ROSAT* band, and the third one approximately corresponding to the *Ginga* or ASCA band.
5. Calculation of X-ray emission in these bands from the three gaseous species separately.
6. Calculation of "observable" temperatures of the X-ray–emitting gas (i.e., those which can be derived from comparing X-ray fluxes in different energy bands) as well as actual temperatures (i.e., obtained as a solution of the hydrodynamical equations) of the gas contributing the bulk of the total X-ray emission in each band.

We study how the outflow from a commencing burst of star formation affects the gas in the disk and the halo of the galaxy on a timescale over which the size of the windblown superbubble becomes comparable to or even exceeds the size of the parent galaxy. We also investigate how, in its turn, the wind is shaped by this gas. From comparing the calculated X-ray emission of different gaseous constituents with the observed X-ray emission of starbursts, we derive conclusions regarding the nature and state of the X-ray emitting material. Properties of the shocked disk gas entrained by the wind and carried far out into the galaxy halo have enabled us to make preliminary inferences as to the origin of extranuclear optical emission-line clouds.

As a template for our model we take the starburst galaxy M82. Since TI and MD also modeled this galaxy, we will be able to compare our results with those in these two papers. However, the major goal of the paper is to gain a deeper insight into the physics of galactic winds in conjunction with the general properties of starbursts rather than to provide a detailed model of M82.

2. DESCRIPTION OF THE MODEL

2.1. *Hydrodynamical Equations*

The axially symmetric gaseous component, which includes the wind material as well as the gas in the galaxy disk and halo, will be described by the following set of equations (cf. TI):

$$\frac{\partial(\rho X_d)}{\partial t}+\frac{\partial}{\partial z}(\rho X_d v_z)+\frac{1}{r}\frac{\partial}{\partial r}(r\rho X_d v_r)=0\,, \tag{1}$$

$$\frac{\partial(\rho X_h)}{\partial t}+\frac{\partial}{\partial z}(\rho X_h v_z)+\frac{1}{r}\frac{\partial}{\partial r}(r\rho X_h v_r)=0\,, \tag{2}$$

$$\frac{\partial(\rho X_w)}{\partial t}+\frac{\partial}{\partial z}(\rho X_w v_z)+\frac{1}{r}\frac{\partial}{\partial r}(r\rho X_w v_r)=\dot{\rho}_{\rm SN}\,, \tag{3}$$

$$\frac{\partial\rho}{\partial t}+\frac{\partial}{\partial z}(\rho v_z)+\frac{1}{r}\frac{\partial}{\partial r}(r\rho v_r)=\dot{\rho}_{\rm SN}\,, \tag{4}$$

$$\frac{\partial}{\partial t}p_z+\frac{\partial}{\partial z}(p_z v_z)+\frac{1}{r}\frac{\partial}{\partial r}(rp_z v_r)=-\frac{\partial P}{\partial z}-\rho\frac{\partial\phi}{\partial z}\,, \tag{5}$$

$$\frac{\partial}{\partial t}p_r+\frac{\partial}{\partial z}(p_r v_z)+\frac{1}{r}\frac{\partial}{\partial r}(rp_r v_r)=-\frac{\partial P}{\partial r}-\rho\frac{\partial\phi}{\partial r}+\frac{\rho v_\phi^2}{r}\,, \tag{6}$$

$$\frac{\partial}{\partial t}p_\phi+\frac{\partial}{\partial z}(p_\phi v_z)+\frac{1}{r}\frac{\partial}{\partial r}(rp_\phi v_r)=-\frac{\rho v_r v_\phi}{r}\,, \tag{7}$$

$$\frac{\partial\epsilon}{\partial t}+\frac{\partial}{\partial z}[(\epsilon+P)v_z]+\frac{1}{r}\frac{\partial}{\partial r}[r(\epsilon+P)v_r]=-\frac{\partial\phi}{\partial z}p_z-\frac{\partial\phi}{\partial r}p_r-\Lambda+\dot{\epsilon}_{\rm SN}\,, \tag{8}$$

with

$$X_d+X_h+X_w=1\,, \tag{9}$$

$$\epsilon=\frac{P}{\gamma-1}+\frac{\rho}{2}(v_z^2+v_r^2+v_\phi^2)\,,$$

$$p_z=\rho v_z\,,\quad p_r=\rho v_r\,,\quad p_\phi=\rho r v_\phi\,, \tag{10}$$

$$\gamma=\frac{X_d C_{Pd}+X_d C_{Ph}+X_d C_{Pw}}{X_d C_{Vd}+X_d C_{Vh}+X_d C_{Vw}}\,, \tag{11}$$

where ρ and ϵ are the mass and energy densities of the gas, respectively, P is the gas pressure, v_r, v_ϕ, and v_z are velocity components, $\dot{\rho}_{\rm SN}$ and $\dot{\epsilon}_{\rm SN}$ are mass and energy input from supernovae and stellar winds of massive stars, Λ represents the radiative cooling (Raymond, Cox, & Smith 1976), and ϕ is the gravitational potential. Here X_d, X_h, and X_w are the mass fractions of the disk, halo, and wind gas, respectively. The identity (9) is preserved up to machine accuracy because of conservative differencing. The mass fractions are advected quantities, and the use of a contact discontinuity steepener (see Collela & Woodward 1984) ensures that their profiles are represented with two-zone accuracy throughout the computation. For the purpose of computation, specific heats for different gas species, C_P and C_V, are held constant. The typical temperature of the wind component is much higher than the galactic virial temperature, so the wind motion is not significantly affected by the gravity. It is affected, however, by the confinement provided by ambient disk and halo gas whose distribution and motion is governed by the gravity field. Therefore the latter is also included into hydrodynamical equations. To solve the above equations, we use the RIEMANN code being developed by one of us (DB) at JHU. For the purposes of this calculation we restrict the three-dimensional code to a $2\frac{1}{2}$ dimensional form. The particular version of the code used here involves the Piecewise Parabolic Method of Collela & Woodward (1984). Since the computations were started a while ago, more recent algorithms, Balsara (1994a, b), have not been used in this round of computations.

We use the multicomponent hydrodynamical description to

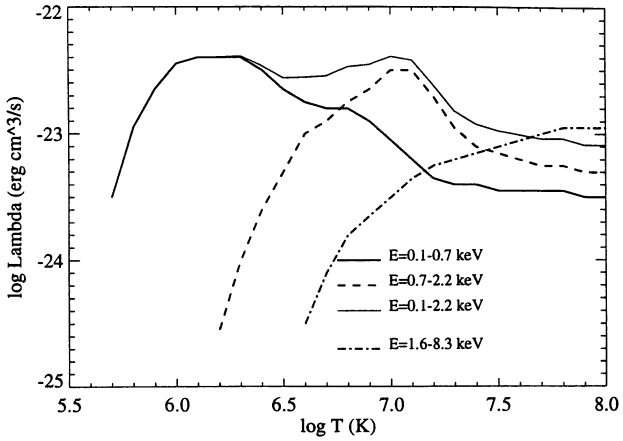

FIG. 1.—Specific X-ray emissivities of hot gas in energy bands considered in the paper.

evaluate the contribution of each gaseous component to the total X-ray flux in three energy bands (see Fig. 1) and to assess the role of each component in the evolution of galactic winds.

2.2. *Gravitational Field*

We assume that in galaxies similar to M82 the major contribution to the gravitational field in the region where the galactic wind propagates comes from a spherically symmetric stellar component. For the sake of generality, we also make allowance for a dark halo component which might be essential at large distances.

The adopted total density distribution of the stellar spheroid and dark halo is

$$\rho_{\rm tot} = \frac{\rho_1}{[1 + (R/r_{c1})^2]^{3/2}} + \frac{\rho_2}{1 + (R/r_{c2})^2}, \quad (12)$$

where the first and the second terms on the right-hand side represent the contribution of stars and dark halo matter, respectively, with $\rho_1 = 1.046 \times 10^{-22}$ g cm^{-3}, $r_{c1} = 385$ pc, and $\rho_2 = 1.257 \times 10^{-22}$ g cm^{-3}, $r_{c2} = 222$ pc. This density distribution of the gravitating material is of the same form as that in TI.

The gravity potential corresponding to the adopted total density distribution is

$$\phi = \phi_1 + \phi_2, \quad (13)$$

where

$$\phi_1 = -4\pi G \rho_1 r_{c1}^2 \frac{\ln\{(R/r_{c1}) + [1 + (R/r_{c1})^2]^{1/2}\}}{(R/r_{c1})}, \quad (14)$$

$$\phi_2 = -4\pi G \rho_2 r_{c2}^2 \left\{0.5 \ln\left[1 + (R/r_{c2})^2\right] + \frac{\tan^{-1}(R/r_{c2})}{(R/r_{c2})} - 1\right\}. \quad (15)$$

The central densities and core radii of the stellar component and dark halo have been chosen by fitting the rotation speed implied by this potential to the rotation curve derived by Nakai et al. (1987) for the inner part of the M82 disk.

For one of our models (see model A2 below) we have added to the above gravitational field the gravity of a thin exponential disk representing the stellar disk of the galaxy. The disk is characterized by a central surface density ($\sigma_0 = 100\ M_\odot$ pc^{-2}), a vertical exponential scale height which has been adopted to be the same at all radial distances ($z_{\rm st} = 100$ pc), and a radial exponential scale length ($r_{\rm st} = 1.5$ kpc). The vertical density distribution for that disk has been truncated at two exponential scale heights. The maximal circular velocity for an exponential disk, $v_{\rm max} = 0.879\pi G r_{\rm st} \sigma_0$, is in this case $v_{\rm max} \approx 55$ km s^{-1}, which is about a factor of 2 smaller than the maximal circular velocity that corresponds to the gravitational field of the stellar spheroid. Therefore, although this stellar disk substantially contributes to the disk-halo gaseous equilibrium, the large-scale density distribution of the galaxy gaseous component in general is dominated by the gravitational field of the stellar spheroid, like for the rest of our models.

2.3. *Gaseous Components and Mass and Energy Injection Rates*

Below we discuss a number of features of the input physics which seem to be among the prime factors determining the observed morphology and emission of the starburst wind regions.

The amount and structure of gas in the disk and halo of starbursts is crucial for the development of galactic winds. The dynamical role of this gas is to provide collimation and confinement for the hot outflow, and also this gas may represent the bulk of the X-ray and optical emitting material. There are at least two different gaseous constituents in the preburst galaxy which may affect the wind and manifest themselves observationally in different ways as they interact with the wind. These are the relatively dense gas in the galactic disk and hot tenuous gas in the halo. An important role may also be played by gas clouds embedded in the pervasive diffuse gas in the disk and the halo of the starburst (e.g., HLA). In fact, this is generic for all situations where interaction of astrophysical shocks and outflows with ambient gas is involved (cf. Hartquist & Dyson 1993): supernova remnants (e.g., Cowie, McKee, & Ostriker 1984), stellar wind bubbles (e.g., McKee, Van Buren, & Lazareff 1984), planetary nebulae (e.g., Dyson 1993), and circumgalactic envelopes around nascent galaxies (e.g., Berman & Suchkov 1991). However, the complexity of cloud—ambient gas interaction, and difficulties in describing the multicomponent cloud—ambient gas medium in terms of hydrodynamical equations (see, e.g., Berman & Suchkov 1991; Arthur, Dyson, & Hartquist 1993) introduces tremendous complications into the quantitative description of galactic winds, which makes a step-by-step approach with a gradually increasing degree of complexity the only reasonable way to incorporate gas clouds into superwind models.

In this paper we will therefore consider the preburst galactic gas as consisting of only two distinct components which represent the gaseous disk and halo, respectively. We shall briefly discuss a role of gas clouds in connection with one of our models in which the material of the gaseous disk above the region of the star formation burst is torn up by the wind into separate dense shreds very early after the onset of the burst, the subsequent development being very much like the one that may be expected for wind–cloud interaction. A detailed analysis of the effects of wind–cloud interaction in the dynamics and X-ray emission of winds in starburst galaxies will be however given elsewhere.

The effect of the ambient gas upon the wind is directly related to the mass of the gas and its distribution. The density distribution in a given gravity field depends on the relative amount of pressure support and centrifugal support, which can be characterized by a parameter e^2 representing the fraction of

the gravity force balanced by the centrifugal force according to equation

$$v_\phi(r) = \left(e^2 r \frac{\partial \phi}{\partial r}\right)^{1/2} . \quad (16)$$

There is little knowledge about the kinematics of gaseous halos of disk galaxies. It seems reasonable to assume that, at temperatures close to the galaxy virial temperature, most of the gravity is balanced by thermal pressure, which would produce a nearly spherically symmetric halo. Such a halo can also be produced by a system of gas clouds whose random velocities correspond to virial equilibrium. In the model of TI there is a large mass of gas residing high above the plane of the disk (i.e., in the galaxy halo). However, this gas shares the dynamics of the disk gas, since it is assumed to be supported almost entirely by rotation, with the rotation speed independent of z coordinate (e = const = 0.9). This assumption of centrifugal support leads to a very special gas distribution. Above a few hundred of parsecs it represents in fact a funnel with dense, massive conic walls confining a low-density region, the latter extending far into the halo along the galaxy minor axis (see TI's Fig. 1). As emphasized by Tomisaka & Bregman (1993), this structure may act at large heights as a very strong collimator for a hot outflow. Although a bipolar flow structure can also develop in a plane-stratified system, the funnel in TI's model may play a crucial role in determining large-scale morphology of the wind region, especially on advanced stages of wind development. The reality of such a preexisting collimator seems rather problematic. In fact, the latter is a result of the oversimplified representation of galactic ISM as a one-component gaseous disk instead of an actually two-component disk-halo structure with kinematically distinct components: a rapidly rotating thin disk and slowly or nonrotating halo. Another disadvantageous consequence of a single-disk ISM model is an unrealistically large gas density far above the plane of the disk. For example, at $z = 1$ kpc, $r = 700$ pc the density in the TI's models is $n \sim 1$ cm^{-3}, which can be compared to $\sim 2 \times 10^{-2}$ cm^{-3} for the same z in the solar neighborhood of our Galaxy according to the density distribution derived by Danly et al. (1992) for the cloudy halo gas. This very dense high-z gas provides tremendous resistance to the wind in the galaxy halo, which leads to a strong reduction in the wind expansion time and increase in the wind density. As a result, the predicted size of the wind region at each particular moment would be strongly underestimated, and the X-ray luminosity of the wind material would be strongly overestimated.

Tomisaka & Bregman (1993) improved TI's model for the galaxy gaseous component by introducing rotational velocity that decreases with increasing z. However, Figure 1*a* in that paper shows that the resulting gas distribution still retains a strong collimating funnel.

Incorporating of a two-component, kinematically distinct disk-halo structure for the galaxy ISM is thus a next logical step to make to progress in understanding and quantitative description of galactic superwinds. The morphology and emission of the wind region observed at any particular time depends not only on the instantaneous mass and energy injection rates but also on the history of mass and energy deposition in the starburst center. The currently observed supernova-dominated galactic winds in galaxies like M82 were plausibly preceeded by much milder hot outflows produced by a cumulative effect of stellar winds from an ensemble of massive stars at the beginning of the star formation burst (cf. Leitherer, Robert, & Drissen 1992, hereafter LRD). These early stellar-wind–powered outflows (lasting for the first few million years) may predetermine the wind dynamics at the wind later, violent supernova-dominated stages. For example, the cavities produced by them in the galaxy gaseous envelope will enable the hot gas injected during the supernova dominated phase to freely escape along the minor axis, thus allowing the wind to impart much less momentum and energy to the dense inner parts of the galaxy. So without elucidating the issue of these early winds we cannot be certain about whether particular superwind models, both quantitative and qualitative ones, have any relevance to real starbursts.

Below we shall examine four models with very different gas components and very different input parameters for deposition of mass and energy in the starburst region (see Table 1), in order to address a few specific issues related to the above discussion. All models have a two-component disk-halo structure, with both the disk and halo gas assumed to be isothermal. The disk component is assumed to be supported mainly by rotation, $e = 0.9$, while the halo gas is considered as entirely pressure supported, $e = 0$. The latter condition does not lead to a collimating funnel far in the galaxy halo, in which respect our model strongly differs from that in TI. The gas densities in the galaxy halo are also far less in our models than in TI (see, e.g., Fig. 2).

All our models have the same parameters for the region where deposition of mass and energy from supernovae and stellar winds takes place, $r = 150$ pc and $|z| = 25$ pc (i.e., the disk 300 pc in diameter and 50 pc thick), which are coincident

TABLE 1

ADOPTED PARAMETERS FOR THE GASEOUS COMPONENTS

Case (1)	n_0 (cm^{-3}) (2)	T_{disk} (K) (3)	T_{halo} (K) (4)	z_{disk} (pc) (5)	H_{disk} (pc) (6)	log M_{halo} ($M_\odot$) (7)	log n_{halo} (cm^{-3}) (8)
A1.....	4	6×10^4	2×10^6	160	160	7.8 (4.2 × 4.2 kpc)	−1.9
A2.....	20	6×10^4	2×10^6	160	500	7.5 (3 × 5 kpc)	−1.8
B1.....	2	6×10^4	2×10^6	160	210	2.9 (2 × 4 kpc)	−2.1
B2.....	12	1×10^4	2×10^6	60	230	5.6 (2 × 4 kpc)	−3.2

NOTES.—Col. (2): The disk initial central density is n_0. Col. (5): z_{disk} is the disk exponential height scale. Col. (6): H_{disk} is the height of the boundary between the disk and the halo at $r = 0$. Col. (7): The halo mass, M_{halo}, is given for the regions ($r \times z$ kpc, with r and z being the region radius and half height, respectively) for which X-ray luminosity has been calculated for the time moments discussed in detail in text (8.3 Myr for model A1, 16.6 for model A2, and 2.0 Myr for models B1 and B2). Col. (8): The mean density of the halo gas in the region indicated in col. (7).

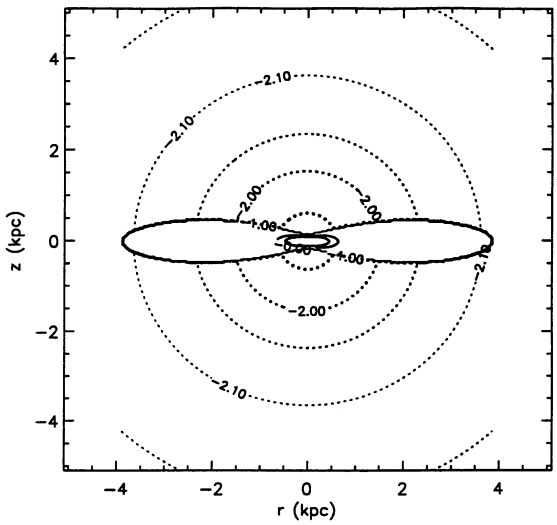

FIG. 2.—Initial density distribution in model A1. Contours are labeled by $\log n\ \mathrm{cm}^{-3}$.

with the ones adopted by TI. The deposited mass and energy is uniformly distributed within this region over several computing zones.

The input parameters for the disk-halo gaseous components are given for different models in Table 1. We specify the gas disk-halo structure of the preburst galaxy by the disk central density, n_0, temperatures of both components, $T_{\rm disk}$ and $T_{\rm halo}$, and the height of the disk at $r = 0$, $H_{\rm disk}$. In choosing $T_{\rm disk}$ and $T_{\rm halo}$, we follow TI and Tomisaka & Bregman (1993). In a real galaxy, much of the hydrostatic support of the interstellar gas is provided by the random "turbulent" motions of the interstellar clouds. Since our simulations do not contain a cloudy component, we have represented the turbulent support by setting the temperature of the gas such that its sound speed is equivalent to the desired velocity dispersion of the system of interstellar clouds. In the case of the disk gas, we have adopted a velocity dispersion of $v \sim 35$ km s^{-1}, corresponding to $T \sim 6 \times 10^4$ K. We have also run one model (B2) in which the disk is assumed to have a temperature of 10^4 K (corresponding to a velocity dispersion of ~ 14 km s^{-1}). In the case of the halo, we have set its temperature to 2×10^6 K (corresponding to a velocity dispersion of ~ 200 km s^{-1}). This implicitly assumes that the interaction of the wind with a system of cold turbulent clouds will be similar to the interaction of the wind with a pervasive hot medium containing the same total mass. We adopt here this implicit assumption (following TI and Tomisaka & Bregman 1993). We will leave a detailed examination of the validity of this assumption to our next paper, where we will explicitly consider a cloudy ISM.

The height of the disk, $H_{\rm disk}$, determines the boundary separating the disk material from the halo gas and should not be confused with the exponential disk scale height. The latter is a few times smaller than the adopted values of $H_{\rm disk}$, depending on the disk gas temperature. At the boundary the two components are in pressure equilibrium. The condition of pressure equilibrium allows us to specify the shape of the disk and fix the equilibrium density distribution in both the disk and the halo once n_0, $T_{\rm disk}$, $T_{\rm halo}$, and $H_{\rm disk}$ as well as the gravity field of the system and the amount of centrifugal support of the gaseous disk and halo are set.

Model A1 is intended mainly to elucidate the effects of time-dependent mass and energy deposition in the starburst region as well as the effects of a two-component structure of the ambient gas. It has an extended halo of a low-density gas, and incorporates time-dependent deposition rates from the LRD stellar population evolution model with star formation rate $2\ M_\odot$ per year for a Salpeter IMF extending from 1 to $120\ M_\odot$. By the time of ~ 17 Myr the resulting stellar population in this model has a bolometric starburst luminosity of $\sim 1.1 \times 10^{44}$ ergs s^{-1}. This can be compared with the total infrared luminosity of M82 of $\sim 10^{44}$ ergs s^{-1}. We have run model A1 for ~ 17 Myr. This is close to the age of active star formation reported by Bernlöhr (1993) for strong starbursts. Thus, we can trace the wind development from the very beginning of the enhanced star formation up to its very advanced stages, and answer the question whether we can have bipolar winds in "mature" starbursts without initially built-in collimating funnels like those in TI. We can also draw conclusions in regard to the role of a low-density halo gas (as opposed to the unrealistically high-density gas far above the galactic plane in TI) in shaping the wind geometry and producing X-ray emission.

Model A2 has the same mass and energy deposition history as in model A1 but differs from the latter in two major respects. First, due to a 5 times larger central gas density and more than 3 times larger disk thickness (at $r = 0$), it has a much higher mass of dense gas right above the region of the star formation burst. This enables us to examine how the ambient gas mass loading affects wind dynamics and X-ray emission. Second, the model allows for the stellar disk gravity, so the disk-halo set-up involves in this case the gravity of both the spheroidal and disk stellar components. This enables us to get an idea as to the extent to which the global structure of the gaseous disk may be important for the wind development.

Model B1 has the same constant mass and energy injection rates as those in TI (except D and F cases): $\dot{M} = 1\ M_\odot$ yr^{-1}, and $\dot{E} = 10^{50}$ ergs yr^{-1}. Its gas distribution is very different from TI, however. It has a low-density spherically symmetric gaseous halo above a thin disk of dense gas, with the gas density distribution in both components providing pressure equilibrium at the boundary between the disk and the halo. This disk-halo structure is essentially the same as in model A1. Model B1 allows us to check whether preexisting funnels in the ambient ISM are actually important for collimation of hot outflows occurring at the mass and energy injection rates typical for M82-type galaxies. The other goal pursued by this model is to gain a better understanding of the X-ray emission caused by winds interacting with a gaseous environment which is probably more realistic than that in TI's model.

Model B2 has been designed to study the wind development in the case of an extremely tenuous halo which is essentially incapable of providing any substantial confinement to the wind. It has also enabled us to draw tentative conclusions in regard to the role of gas clouds in producing X-ray emission in the starbursts. The importance of modeling dramatically different gaseous halos is associated with the fact that there still is a severe deficiency of concrete data on the gaseous content of galactic halos in general. There is also a plausibly wide range for the halo gas mass and density in real starburst galaxies. As compared to model B1, model B2 has 6 times larger central density for the disk gas and about one order of magnitude less massive, less dense gaseous halo. This difference from model B1 is achieved by substantially reducing the scale height for the disk gas, $z_{\rm disk}$, while keeping the boundary between the disk and the halo at the same vertical distance from the center, $H_{\rm disk}$, as in model B1 (see Table 1).

For all our models we have calculated the X-ray emission of the wind and wind-shocked disk and halo gas. The unperturbed halo gas has not been included, since we assume that in a real galaxy the actual kinetic temperature of the unperturbed halo gas is much less than the value of 2×10^6 K which we have used in our simulations to represent the hydrostatic support provided by a turbulent velocity dispersion of ~ 200 km s^{-1} (see the discussion above). The calculations have been done for three different energy bands, 0.1–0.7 keV, 0.7–2.2 keV, and 1.6–8.3 keV. The emission in the 0.1–2.2 keV band has also been calculated. Specific X-ray emissivities for these calculations (Fig. 1) have been derived from Raymond et al. (1976). The first two bands can be used as a temperature diagnostic for the soft–X-ray emitting material. They will be referred to as the "soft" bands, and the same will be applied to the entire band 0.1–2.2 keV. The bands can be isolated, e.g., in *ROSAT* spectrometric data (0.1–2.4 keV). For example, the *ROSAT* observations of NGC 253 made by Pietsch (1993) have used three bands: 0.1–0.5 keV, 0.5–1.0 keV, and 1.0–2.4 keV. The first one is pretty close to our 0.1–0.7 keV band while the results for our band 0.7–2.2 keV can be compared to those obtained by summation of fluxes from the 0.5–1.0 keV and 1.0–2.4 keV bands.

The results for the 1.6–8.3 keV band can be compared to the data obtained by the X-ray observatories *Ginga* which measures much harder emission, 2–20 keV, and BBXRT and ASCA which have the capability of performing spectroscopy across the 0.5–10 keV band. The emission in the 1.6–8.3 keV band will be referred to as the "hard" X-ray emission.

3. NUMERICAL RESULTS

3.1. *Model A1*

Figure 2 shows the initial density distribution for model A1. This is the model with continuous star formation in which deposition of mass and energy in the starburst region is dominated over the first ~ 5 Myr by stellar winds from massive stars, and after that time the supernovae take over the role of major depositors. So by a time of 8.3 Myr, displayed in Figures 3–7, we can observe the effects of both stellar and supernova mass and energy injection.

General features of the developing gas flow in model A1 (as well as in model B1—see below) are similar to those described by TI. However, they are substantially modified by presence of two distinct gaseous components. We have a clear-cut bipolar outflow confined by well-defined conic walls (in TI the wind geometry is cylindrical rather than conic). There is an outer shock propagating within the halo gas which has traveled a distance of 3.8 kpc along the minor axis by the time 8.3 Myr. Behind the shocked halo gas we have the shocked gas of the disk material which is followed by the wind material compressed by the internal shock (see Fig. 5).

Figure 6 displays the density distributions of the wind, disk, and halo gas separately. It is clearly seen that the wind is collimated by the dense disk component whose material is being dragged out by the wind to produce and maintain extended walls of a clear-cut biconic cavity. The cavity opening angle is $\sim 70°$. The disk material which initially resided right above the starburst region has been compressed to a thin shell and pushed up far in the halo to form, together with the shocked wind and halo gas, a shell that confines a large bubble of a hot, extremely rarefied gas. The wind is freely streaming outward within the biconic cavity up to ~ 2.6 kpc and is stopped there by the internal (reverse) normal shock in the wind material (see Fig. 7). The cavity side walls seen in the left panel in Figure 6 represent substantially denser material of the entrained disk gas which is mixing and flowing upward with the wind gas (Fig. 8). The front of the internal normal shock stretches essentially horizontally over ~ 1.5 kpc. At its ends the hot gas breaks through and streams out, whirling in a large cavity behind the walls of the central biconic cavity. This is clearly seen in the left panel of Figure 7.

This complex behavior eventually results in a correspond-

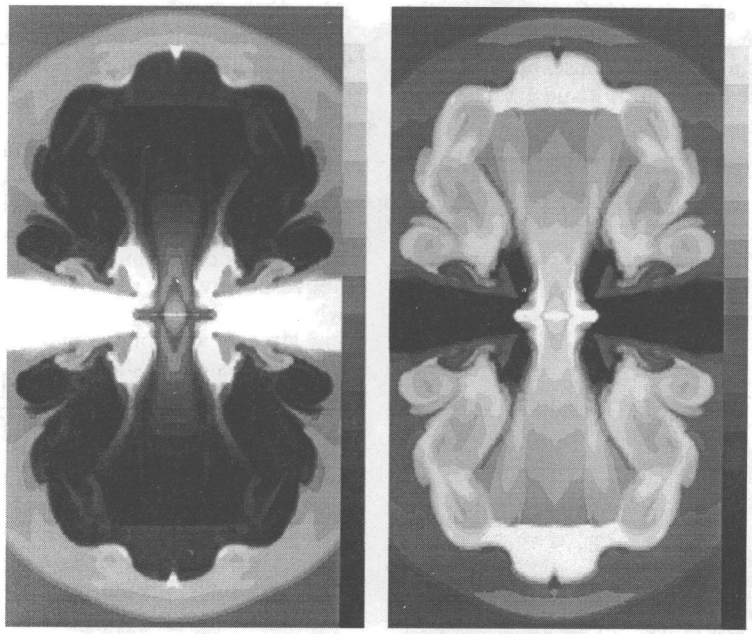

FIG. 3.—Gray-scale representation of the density (*left panel*) and temperature (*right panel*) distributions in model A1 at 8.3 Myr in the central $r - z$ plane of the galaxy. The image size is 4.2×7.8 kpc. The scale is logarithmic, with the log n (cm^{-3}) range $[-3.5, -1.0]$ and log T (K) range [4, 8] (in this and subsequent figures representing gray-scale images, the regions with the parameter values beyond the indicated lower and upper limits are shown as black and white, respectively).

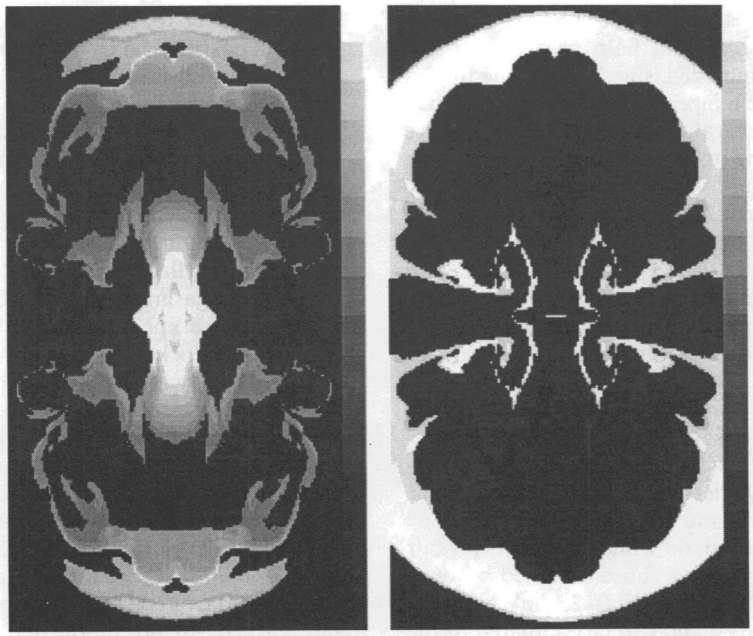

FIG. 4.—Gray-scale representation of the X-ray emissivity distributions of the wind and shocked disk and halo gas for the 1.6–8.3 keV (*left panel*) and 0.1–2.2 keV (*right panel*) energy bands in model A1 at 8.3 Myr. The image size is 4.2 × 7.8 kpc. The scale is logarithmic, with the log f(ergs cm^{-3} s^{-1}) ranges [−28.5, −26.5] and [−25.7, −25.0] for the two energy bands, respectively.

ingly complex flow pattern. The right panel in Figure 7 demonstrates the velocity field at 16.6 Myr. By this time the supernovae have dominated the wind for a long period, and the deposition of mass and energy from them is still further increasing due to continuing growth of the supernova rate (cf. LRD). Several different factors are equally important in these later stages of the wind evolution: wind interaction with the pushed up disk gas, entrainment of the dense disk material from the base of the biconic walls into the main outflow right on the galaxy minor axis, runaway radiative cooling in regions occupied by strongly compressed gas, etc. For example, the "ledge" at $z \approx 0.5$ kpc on the density profile in Figure 5 has developed by 16.6 Myr into a compact dense blob of cold ($T \approx 10^4$ K) gas clearly outlined in Figures 9 and 10. The blob

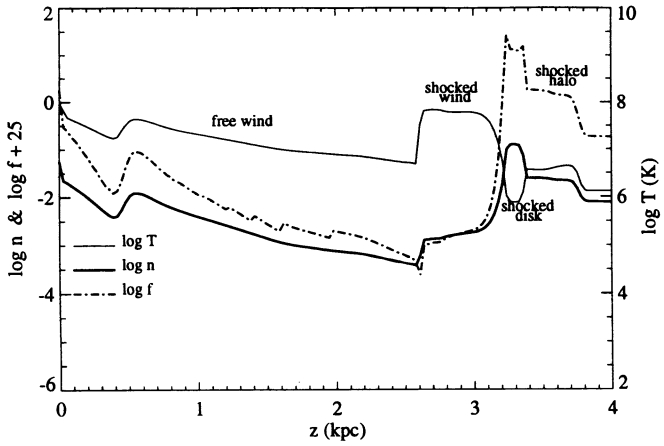

FIG. 5.—Temperature, density, and 0.1–2.2 keV X-ray emissivity profiles along the minor axis at 8.3 Myr in model A1. The units for density and X-ray emissivity are cm^{-3} and ergs cm^{-3} s^{-1}, respectively. The regions occupied by the free wind, shocked wind, shocked halo, and shocked disk material are indicated.

is very dense and cold (Fig. 11), and, as seen in Figure 12, is obviously dominated by the disk gas. We have traced the fate of various pieces of material in the wind region to verify that the blob did really form from the disk material which resided at the time $t \sim 8.3$ Myr at the base of the conic walls seen in Figure 3 and was then partially entrained, together with the adjacent halo gas, into the main stream. This can be seen, for example, in Figure 8. It shows that at 8.3 Myr there is no dense material near the galaxy vertical axis at all, and the dense gas slowly streams along the wall of the biconic cavity. At 16.6 Myr, however, the gas motion around the vertical axis above a few hundred parsecs is clearly dominated by the dense disk gas with a significant velocity component directed toward the axis. That explains how the dense cold blob has appeared right on the galaxy axis.

Figure 12 shows that the wind material and the halo gas also contribute to the blob. As seen from Figure 7, by the time 16.6 Myr the blob blocks the free wind streaming along the minor axis, making the wind skirt it and flow between the blob and dense walls of biconic cavity. After that, the wind crashes from above downward into the "shadow" region above the blob, which is well depicted in the right panel of Figure 7. The colliding streams of upflowing and downflowing gas produce a complex system of shocks and tangential discontinuities which are traced in the density distribution by a net of dense filaments (see left panel in Fig. 9). A substantial fraction of dense disk material, which by 8.3 Myr produced the collimating walls of the biconic cavity (Fig. 6), has been entrained by the wind and carried far into the halo in the form of filaments stretched upward (compare left panels in Figs. 9 and 3).

This picture is obviously more complex than that in the "conventional" scenario for a (spherically symmetric) bubble of hot gas emerging from an actively star-forming region in the galactic disk and expanding into the halo. The difference is due, of course, to the fact that in our case the bubble is initially confined by two very different shells produced by the shocked

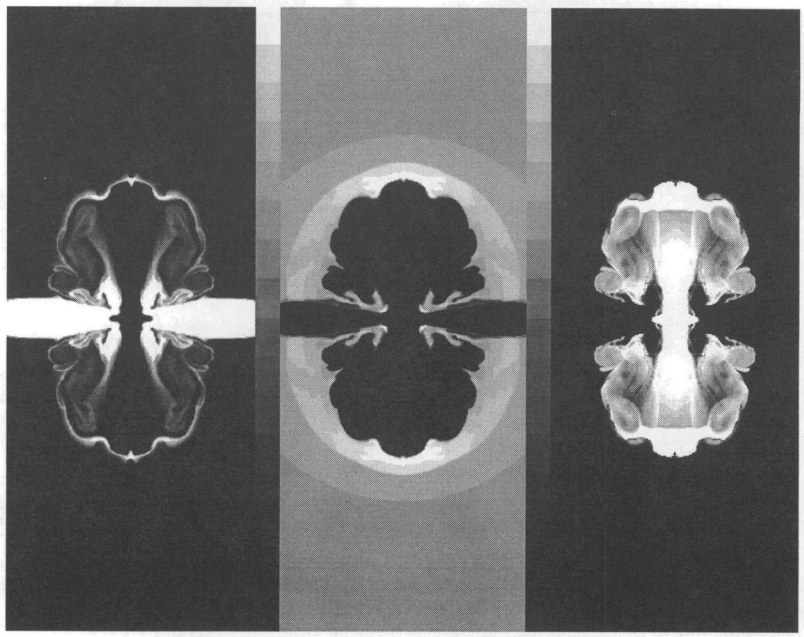

FIG. 6.—Density distribution of the disk gas (*left panel*), halo gas (*middle panel*), and wind material (*right panel*) in model A1 by the time 8.3 Myr (compare with the total density distribution in Fig. 3). The image size is 6 × 15 kpc. The scale is logarithmic, with the log n (cm^{-3}) range $[-4.5, -1.5]$, $[-3.5, -1.5]$, and $[-4.5, -3.0]$ for the three gas components, respectively.

gas in the two very different gaseous components whereas a "conventional" hot bubble is confined by a single shell of compressed one-component ambient gas. In this latter case separate dense clumps and filaments appear only after the "blow-out" occurs, i.e., after the shell of the swept-up ambient gas is disrupted by Rayleigh-Taylor instability and the wind freely streams out. In model A1 the instability disrupts the shell of the dense disk material at a rather early stage of the wind development. However, the subsequent wind flow in that case is not a free streaming since now the wind encounters a resistance provided by the halo gas. The shell of the shocked halo gas remains stable even at very late phases, i.e., a "second" blow-out does not occur, and this shell continues to strongly affect the wind flow. As a result, we have a spectacular filamentary structure of density distribution as well as a conspicuous pattern of whirling motions alongside with a very regular outer shell, which is so different from the picture of a "conventional" bubble.

Let us show that the disruption of the outer thin shell of the shocked disk gas can really be understood in terms of

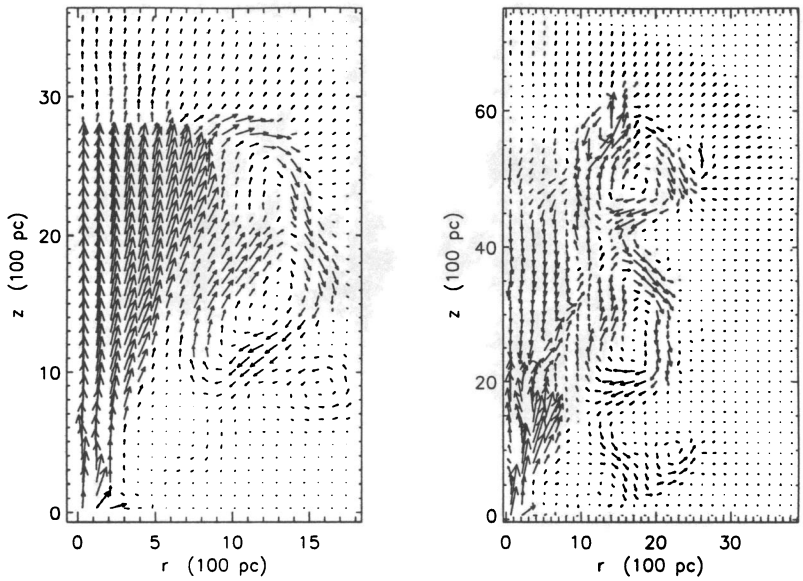

FIG. 7.—Velocity field in model A1 at 8.3 Myr (*left panel*) and 16.6 Myr (*right panel*). The velocity values are binned over three (*left panel*) and five (*right panel*) computing cells, which explains why the arrows on the vertical axis are not always parallel to the latter. The maximal velocity is 2350 and 2175 km s^{-1} for 8.3 and 16.6 Myr, respectively.

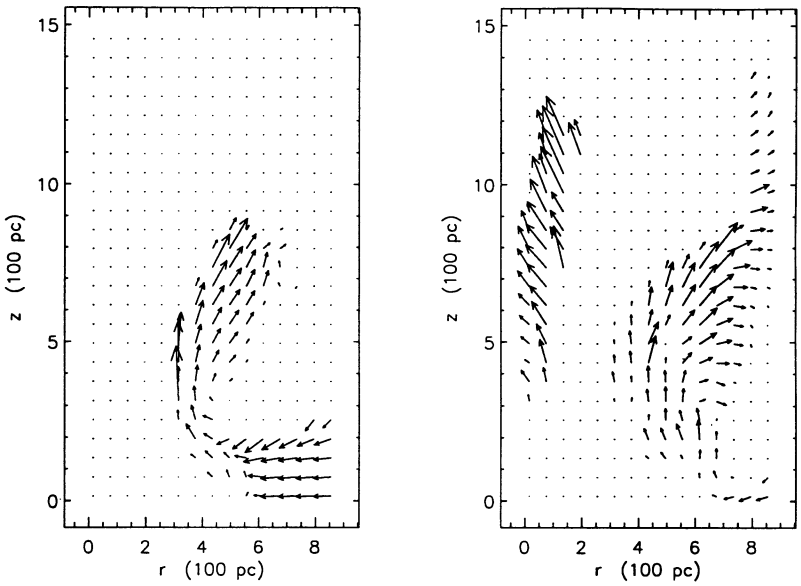

FIG. 8.—Same as in Fig. 7 but for the dense disk gas ($\log n > -1.0$) only. The maximal velocity of this gas is 260 km s^{-1} at 8.3 Myr and 780 km s^{-1} at 16.6 Myr. The velocity values are binned over two computing cells.

Rayleigh-Taylor instability. The dispersion relation for gravity waves in two plane-parallel layers of fluids with densities ρ_1 and ρ_2 is

$$\omega^2 = kg \frac{\rho_1 - \rho_2}{\rho_1 + \rho_2}, \tag{17}$$

where ω is angular frequency, k is wavenumber assumed to be much larger than the layer thicknesses, and g is gravitational acceleration (Landau & Lifshitz 1987). If $\Delta\rho = \rho_1 - \rho_2 < 0$, i.e., if the lighter fluid is below the heavy one, then ω^2 is negative, which corresponds to an unstable situation with the amplitude of gravity waves growing on a timescale of ω^{-1}. Our models are much more complex than a simple case for which the above dispersion relation was derived. However, we may still obtain from the latter the order-of-magnitude estimates of the timescales involved, which would give at least an idea on the role of Rayleigh-Taylor instability in our models. For the time 8.3 Myr, let us apply equation (17) to a segment of the dense shell of disk material laying at the height $z \sim 3$ kpc not far away from the galaxy minor axis. We may estimate gravitational acceleration as $g = v_{\rm circ}^2/z$, where $v_{\rm circ}$ is galaxy circular velocity at a distance z. This yields the Rayleigh-Taylor instability timescale as

$$t_{\rm RT} = (2\pi)^{-1/2}(\lambda z/v_{\rm circ}^2)^{1/2}(\Delta\rho/\rho_{12})^{-1/2}, \tag{18}$$

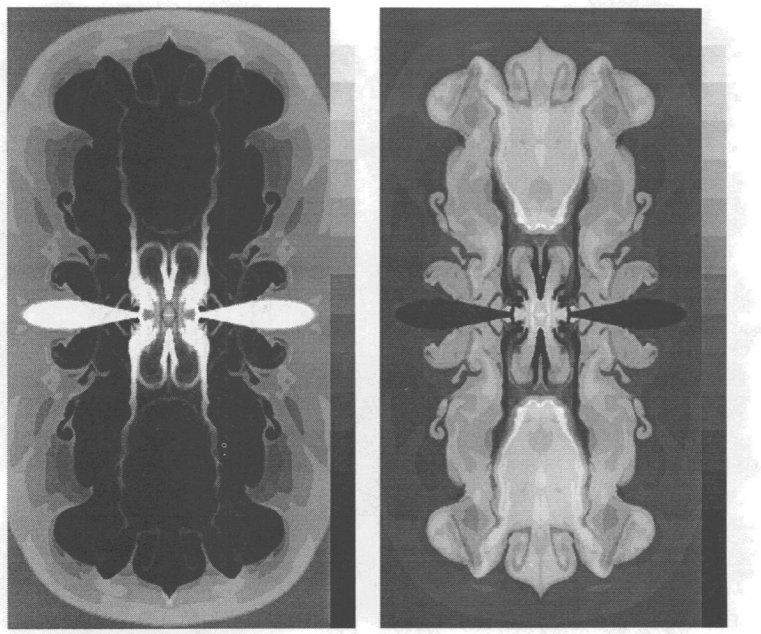

FIG. 9.—Same as in Fig. 3 but at 16.6 Myr. The image size is 7.8 × 15 kpc.

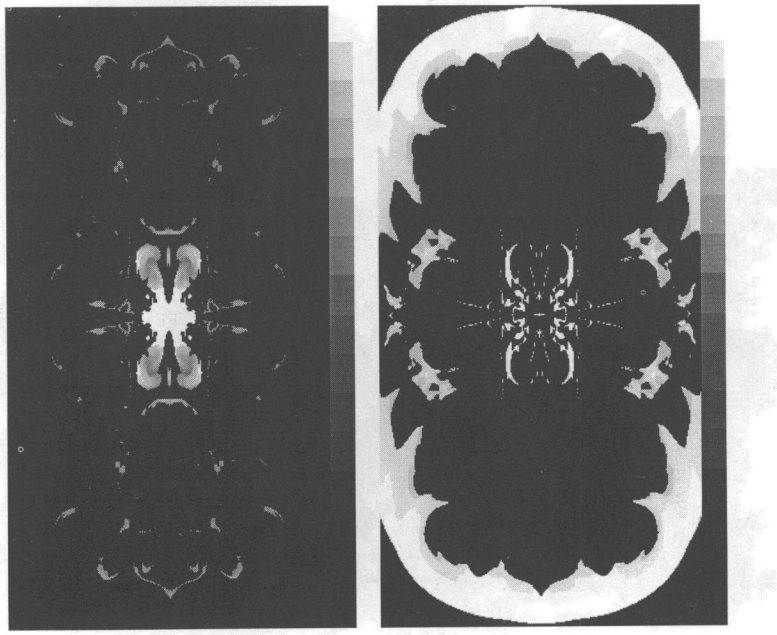

FIG. 10.—Same as in Fig. 4 but at 16.6 Myr. The image size is 7.8 × 15 kpc.

where $\lambda = 2\pi k^{-1}$ and $\rho_{12} = \rho_1 + \rho_2$. As follows from equation (17), the instability increment is smaller for longer wavelengths. However, the wavelengths of perturbations which eventually may disrupt the shell are evidently of the order of the shell thickness, d_{sh}, so we must adopt $\lambda = d_{sh}$ in order to estimate the timescale for shell disruption due to instability. From Figure 5 we see that the shell thickness for the disk material is $\sim$0.2 kpc. The same figure shows that the density difference between the shell and shocked wind gas is slightly less than two orders of magnitude. The circular velocity at $z \sim 3$ kpc is $v_{circ} \approx 100$ km s^{-1} in all our models. With these numbers, equation (18) yields $t_{RT} \approx 3$ Myr. Thus by the time 8.3 Myr we may expect to observe effects of Rayleigh-Taylor instability. The distorted, partially broken shape of the outer thin shell of disk material seen in Figure 6 seems to represent just these effects. As displayed in Figure 12, over next 8.3 Myr, by the time 16.6 Myr, the shell entirely fragments, presumably under the same effects of Rayleigh-Taylor instability, into separate pieces.

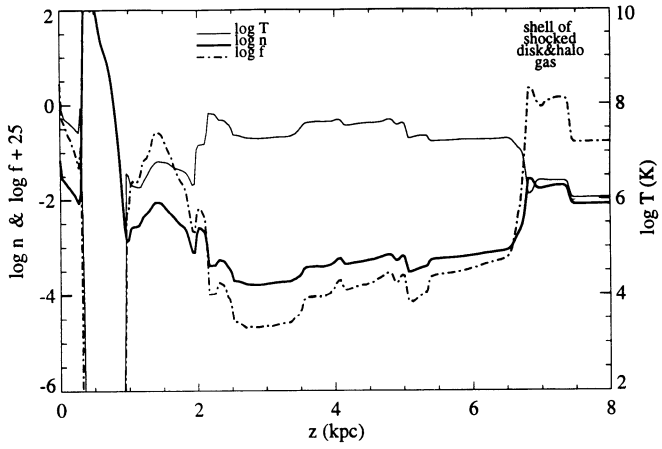

FIG. 11.—Same as in Fig. 5 but at 16.6 Myr

3.2. *Model A2*

A remarkable feature of model A2 is that, unlike the case of model A1, the breakthrough of the hot outflow into the halo occurs obliquely rather than perpendicular to the galactic disk along the galaxy minor axis (Figs. 13 and 14). This is certainly due to a much larger mass of dense gas right above the central region of the starburst which blocks the vertical outflow of the hot gas (compare Figs. 5 and 15). However, despite the striking apparent difference between Figures 9 and 13, there is a remarkable similarity in the topology of the hot outflows in these two models. In fact, the oblique breakthrough and blocking of the direct outflow develops very similarly to that which occurs in model A1 at late stages. The scales of various features in the flow pattern, including the size and the shape of the hot bubble, are, of course, different in models A1 and A2.

This model provides an excellent illustration of the role of dense gas in confining the hot gas in the center of the galaxy. As seen in Figure 13, the radial size of the central region occupied by the supernovae ejecta is few times smaller than that in model A1 at the same moment of time (Fig. 9). This is obviously due to the fact that the initial central density in model A1 is 5 times smaller than that in model A2.

The self-gravity of the stellar disk, which has been included in model A2, does not seem to have a major effect upon the properties of galactic superwinds discussed in this paper. In fact, we should have expected this because the region where the long-term wind behavior is shaped is dominated by the gravity of the stellar spheroid.

3.3. *Model B1*

The development of the hot outflow in model B1 is illustrated by Figures 16–20. Many of the flow features discussed for model A1 are also clearly seen in these figures. However, due to a larger energy injection rate, the wind dynamics in model B1 is much more vigorous than in model A1. Suffice it to say that in model B1 the wind has driven a shock into the halo out to a vertical distance of $\sim$3 kpc in only 2 Myr while in model A1 the same distance has taken the wind $\sim$8 Myr. This

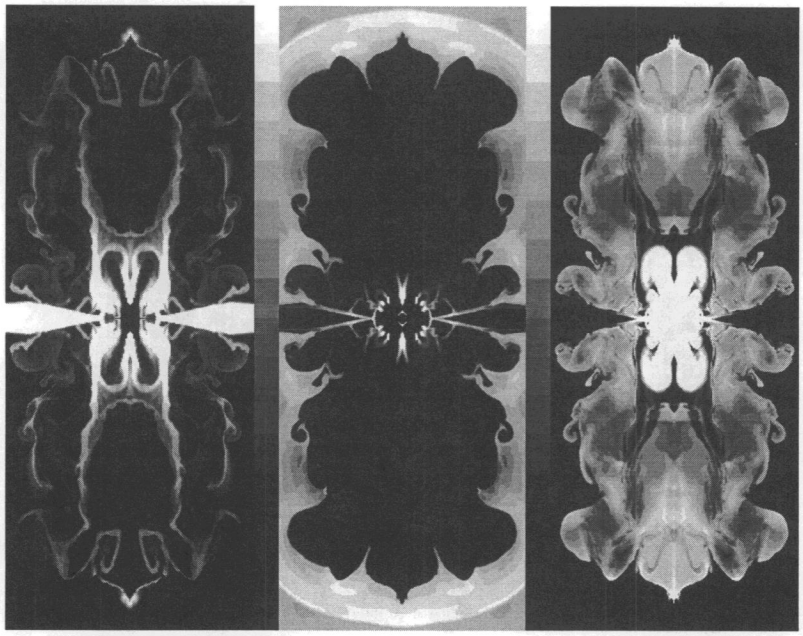

FIG. 12.—Same as in Fig. 6 but at 16.6 Myr. The image size is 7.8 × 15 kpc.

intuitively obvious difference can be described quantitatively in terms of differences in starburst bolometric luminosity (or energy injection rate) and ambient gas density. In a simple spherically symmetric wind model, which can be used for the purpose of order-of-magnitude estimates, equation (9) in HLA (see also Koo & McKee 1992 and references therein) yields the time required for the wind-shocked material (the bubble's shell) to reach the distance $r_{\rm shell}$ as

$$t_{15} = 0.14 \dot{E}_{42}^{-1/3} n_0^{1/3} r_{\rm shell,kpc}^{5/3} , \qquad (19)$$

where $r_{\rm shell,kpc}$ is in units of kpc, $\dot{E}_{42}$ is in units of 10^{42} ergs s^{-1}, t_{15} is time in units of 10^{15} s ($\approx 3.2 \times 10^7$ yr), and the wind is assumed to be "fast" (Koo & McKee 1992). Now, the halo density in model A1 is about a factor of 3 higher than in model B1. For model B1 we have $\dot{E} \approx 3 \times 10^{42}$ ergs s^{-1}. For model A1 the time-averaged value for $\dot{E}$ between 0 and 8.3 Myr is about a factor of 10 smaller, $\dot{E} \sim 3 \times 10^{41}$ ergs s^{-1}. As a result, within model uncertainties, we get a timescale for model B1 that is ~ 3 times shorter than that for model A1, which reasonably agrees with the timescales implied by Figures 5 and 18.

We can also discuss these types of scalings in terms of starburst bolometric luminosity, $L_{\rm bol}$, since the latter quantity seems to correlate pretty well with both energy and mass depo-

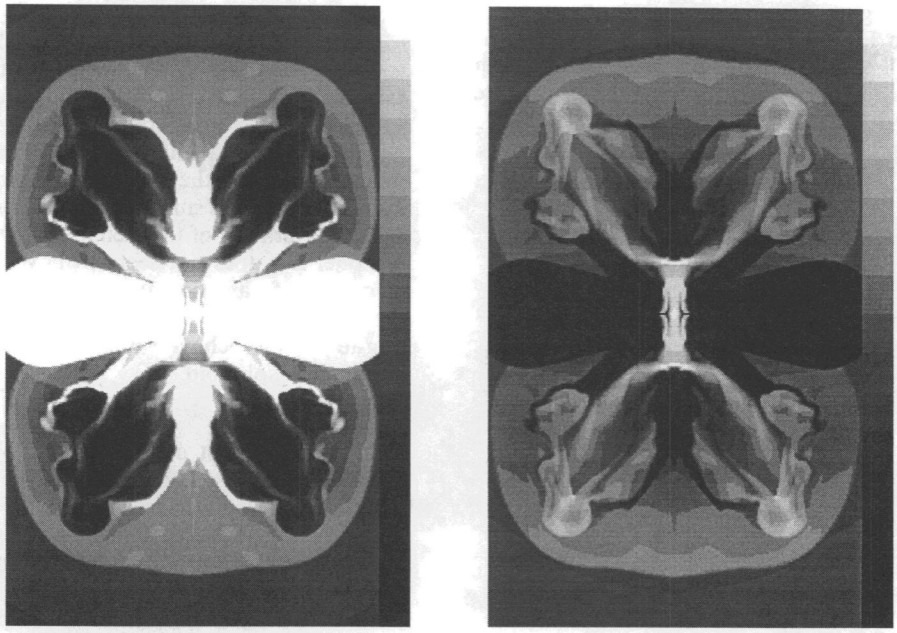

FIG. 13.—Gray-scale representation of the density (*left panel*) and temperature (*right panel*) distributions in model A2 at 16.6 Myr in the central $r - z$ plane of the galaxy. The image size is 6 × 10 kpc. The scale is logarithmic, with the log n (cm^{-3}) range [−3.0, −1.0] and log T (K) range [4, 8].

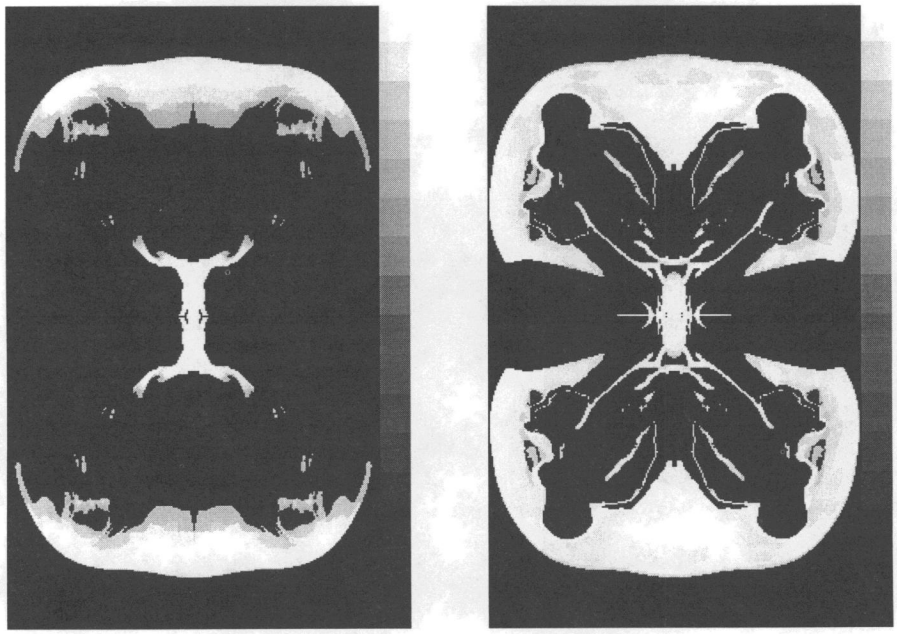

FIG. 14.—Same as in Fig. 4 but for model A2 at 16.6 Myr and the image size 6 × 10 kpc. The range of log f is [−27.5, −23.0] and [−25.7, −23.0] for the two energy bands, respectively.

sition rates. For example, according to HLA,

$$\dot{E} = 8 \times 10^{42} L_{\mathrm{bol},11} \text{ ergs s}^{-1} , \quad (20)$$

$$\dot{M} = 3 L_{\mathrm{bol},11} M_{\odot} \text{ yr}^{-1} , \quad (21)$$

where $L_{\mathrm{bol},11}$ is in units $10^{11} L_{\odot}$.

The wind breakthrough at the ends of the normal internal shock, which was discussed earlier for model A1, also occurs in model B1. This is seen especially well at more advanced evolutionary stages. For example, the velocity field at 3.2 Myr in Figure 19 clearly outlines the biconic flow, with whirling motions developing sideward to the walls of the biconic cavity much like to those seen in Figure 7 for model A1. A more quantitative representation of the velocity field at 3.2 Myr is provided by Figure 20.

3.4. *Model B2*

The much lighter halo of model B2 cannot provide the same confinement of the hot outflow as the halos in three previous models do. Also the smaller scale height of the dense disk material is incapable of providing the wind the same degree of collimation. Therefore the flow pattern beyond the region of free wind is extremely irregular, with spectacular "cometary" blobs of disk material which have been swept away far into the halo (see Figs. 21–23). However, even in this case the wind has an obvious bipolar geometry.

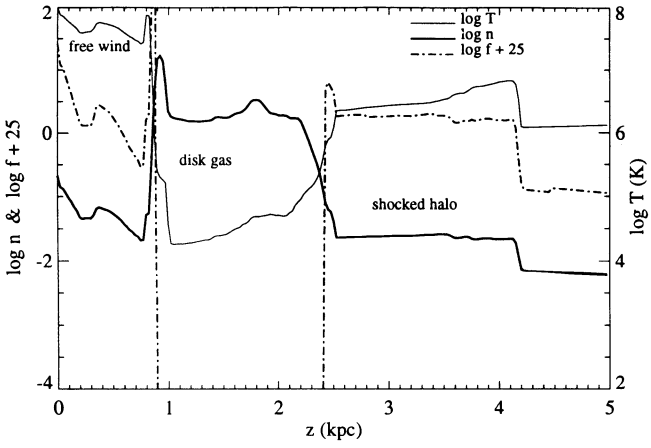

FIG. 15.—Same as in Fig. 5 but for model A2 at 16.6 Myr

Inspection of Figure 21 clearly shows that most of the shocked and swept-away disk gas in this model is torn by the wind into shreds which strongly resemble comets: they have compact dense heads and long tails of less dense material extended outward. The dense gaseous blobs form very early after the onset of the wind and behave like separate clouds as they interact with the latter; even bow shocks, which are typical features of a wind-cloud interaction, are clearly visible in Figure 21. (It should be remembered, of course, that our model is azimuthally symmetric rather than fully three-dimensional, and so are our "clouds"). As a result, the wind streams essentially freely between these "clouds" after a short initial phase and, unlike the case of models A1, A2, and B1, the wind imparts less momentum to the disk material. For example, the average velocity, $v = z/t$, of the dense clump right on the minor axis at $z \approx 1.2$ kpc (see Figs. 21 and 23) is only ~ 650 km s^{-1}, which is to be compared with an average velocity of ≈ 1300 km s^{-1} for the corresponding piece of disk material in model B1.

The instantaneous clump velocity is, of course, larger than the average value indicated above: $v \approx 890$ km s^{-1}. It can be compared with the estimate which one can derive from equation (18) in HLA for a spherically symmetric wind:

$$v_{\mathrm{cloud}} = 140 \dot{E}_{42}^{1/2} r_{\mathrm{kpc}}^{-1/2} N_{21}^{-1/2} \text{ km s}^{-1} , \quad (22)$$

where r_{kpc} is the initial distance from which the cloud gets accelerated and N_{21} is the cloud column density in units of 10^{21} cm^{-2}. Adopting $\dot{E}_{42} = 3.2$, $r_{\mathrm{kpc}} = 0.5$, $n_{\mathrm{cloud}} = 1$ cm^{-3} (which is approximately the average density of the clump that we discuss), and $l_{\mathrm{cloud}} = 0.2$ kpc (which is the clump dimension in radial direction), we obtain $v_{\mathrm{cloud}} = 450$ km s^{-1}. Having in mind that the above equation was derived for spherical clumps

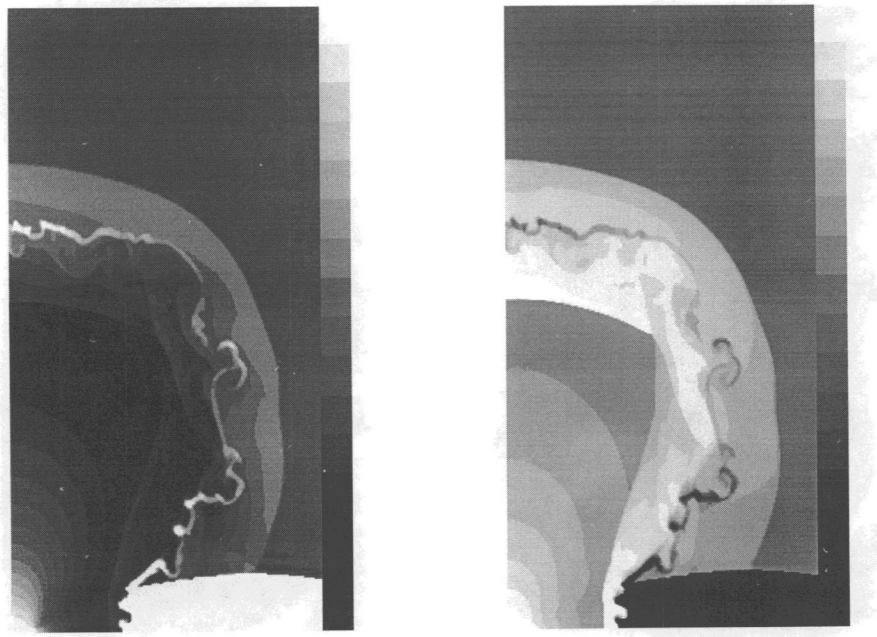

FIG. 16.—Same as in Fig. 3 but for model B1 at 2.0 Myr. The image size is 2 × 4 kpc, the range of log n (cm^{-3}) is [−3.9, −0.8], the range of log T is [4, 8]. Only a quarter of the image is displayed.

and provides in any case only an order-of-magnitude estimate, we conclude that the agreement between the actual clump velocities in model B2 and those estimated from equation (22) is quite reasonable. We can also compare the clump velocity with the velocity range inferred by HAM for dense optical line-emitting clouds in starbursts: $v_{opt} \sim 400$–600 km s^{-1}. The comparison does not rule out the same acceleration mechanism for the line-emitting gas which is responsible for clump velocities in model B2. A larger value of the clump velocity in model B2 can easily be understood in terms of difference in parameters in equation (22).

The comet-like entities seen in Figure 21 seem indeed to have much in common with ordinary comets whose evaporated material is entrained by the solar wind to produce long tails directed radially away from the Sun. Just as in the case of comet–solar wind interaction, the morphology of shreds in Figure 21 is suggestive of ablation of dense lumps of the disk gas and entrainment of the ablated material by the galactic

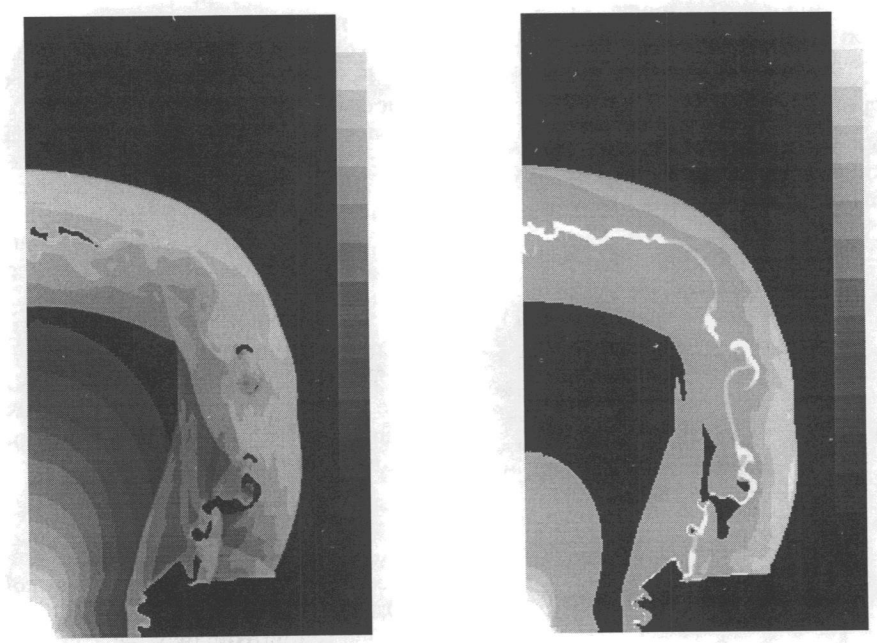

FIG. 17.—Same as in Fig. 4 but for model B1 at 2.0 Myr. The image size is 2 × 4 kpc. The range of log f is [−31.0, −24.5] and [−26.5, −25.0] for the two energy bands, respectively.

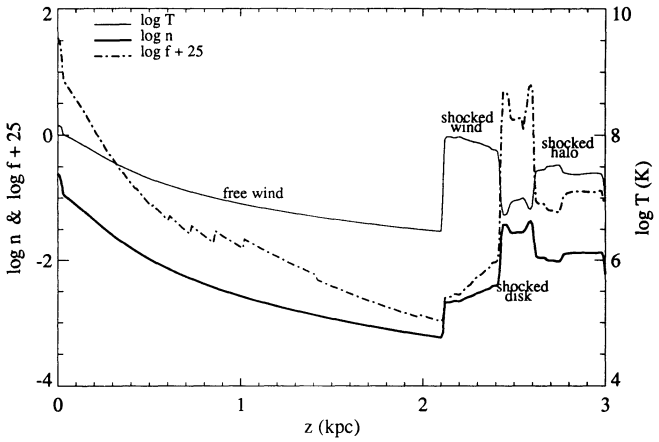

FIG. 18.—Same as in Fig. 5 but for model B1 at 2.0 Myr

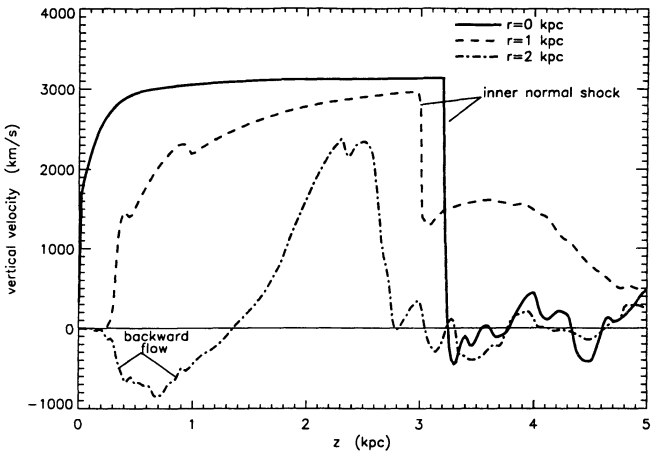

FIG. 20.—Vertical variation of z-component of velocity at the radial distances $r = 0$, 1, and 2 kpc in model B1 at 3.3 Myr.

wind (although in this case the tails are not as regular because of the irregularities in the wind flow induced by wind-cloud interaction). If the simulation were indeed three-dimensional (so that our "comets" were really comet-like blobs instead of rings) the effect would be greatly enhanced.

In general the emerging picture for model B2 appears to be very similar to the one which is expected for wind-cloud interaction. In this respect model B2 gives insight into the situation in which gas clouds in the disk and the halo of the galaxy provide the bulk of X-ray emission as they become shocked and ablated by the wind.

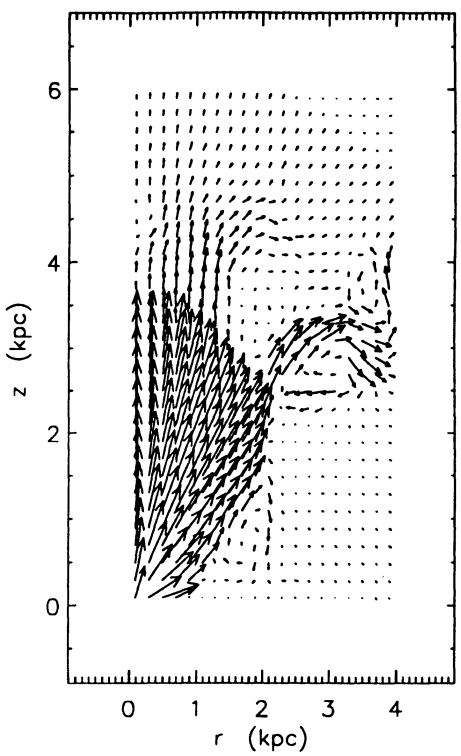

FIG. 19.—Velocity field in model B1 at 3.2 Myr. The maximal velocity is 3130 km s^{-1}.

4. DISCUSSION

4.1. *The Nature of the Soft X-Ray Emitting Material*

For all our models, we have calculated the X-ray emission in different energy bands and derived the mass and effective temperature of the emitting gas (Tables 2–4). Table 2 gives the corresponding parameters for model A1 at 8.3 Myr for the three gaseous components separately. The last line in the Table 2 represents the same parameters but for the integrated contribution of all three components. Similar data for models A1 and A2 at 16.6 Myr as well as for models B1 and B2 at 2 Myr are given in Tables 3 and 4, respectively. The gray-scale representation of the emissivity distribution of the wind and shocked disk and halo gas in the soft band (0.1–2.2 keV) and hard band (1.6–8.3 keV) is given in Figures 4, 10, 14, 17, and 22, in their right and left panels, respectively.

The data in Table 2 imply that in model A *the soft X-ray luminosity of the wind material is negligible in comparison with that of the shocked halo and disk gas.* A similar conclusion was made by Tomisaka & Bregman (1993). They suggested that most of the soft X-ray emission in their models seems to come from the compressed halo material. This inference is to be compared with the conclusion of TI that the observed soft X-ray flux should originate in the free wind region at low z and in the shocked wind matter at high z. As we see, the presence of the hot tenuous halo gas (as opposite to the dense disk gas extended far into the halo in TI's models) can drastically change the site of major soft X-ray production, replacing the wind material as a major X-ray emitter by the shocked disk and halo gas. The prevalence of this material in the production of X-ray emission is sustained over the entire time span involved in our simulations, and from comparison of Figures 5 and 11 one may easily deduce that there is no tendency for a temporal decrease in the shocked disk and halo gas contribution to the total X-ray luminosity.

The dominance of the shocked disk and halo gas in the soft X-ray emission in model A1 can independently be inferred from Figure 24. It shows that essentially all the soft X-ray flux comes from the gas cooler than $\log T \approx 6.3$ and $\log T \approx 6.2$ at 8.3 and 16.6 Myr, respectively. These temperatures are typical for the shocked disk and halo gas, while the temperature of the shocked wind material is more than an order of magnitude larger (see, e.g., Fig. 5).

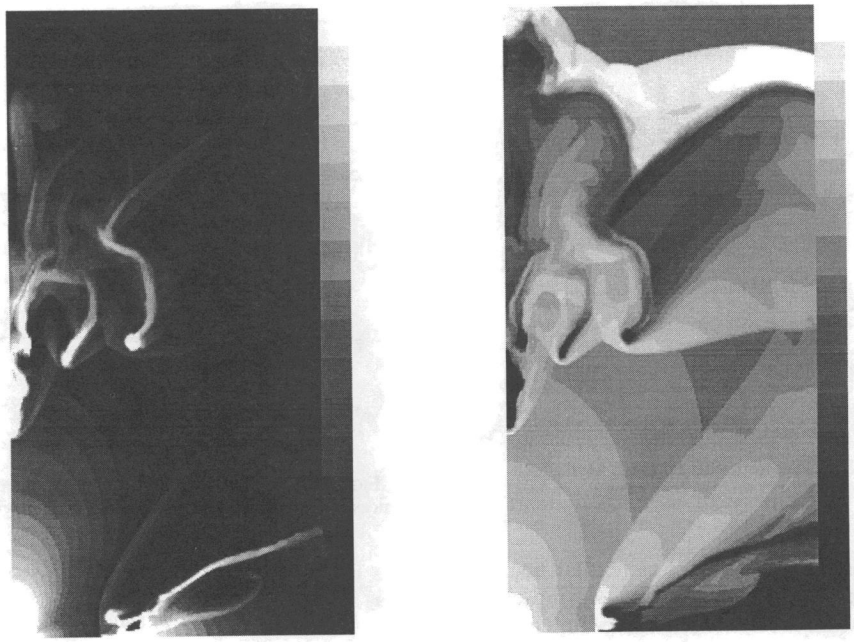

FIG. 21.—Same as in Fig. 3 but for model B2 at 2.0 Myr. The image size is 2 × 4 kpc, the range of log n (cm^{-3}) is [−3.5, −1.5], the range of log T is [4, 8].

The above inference turns out to be true for all our models, which seems quite surprising in view of great differences between the models. As seen in Figure 25, the entire soft X-ray flux in model A2 is coming from the gas at temperatures below log $T = 6.7$, while the wind temperature is $\sim 10^8$ K. Inspection of Figure 26 clearly indicates that the bulk of the soft X-ray emission comes for the gas at temperatures below log $T = 7.0$ and log $T \approx 6.5$ for models B1 and B2, respectively. Again, these temperatures are much lower than the typical temperature of the shocked wind material, log $T \approx 8.0$. However, they agree well with those of the shocked disk and halo gas (see e.g., Figs. 15, 18, and 23). Therefore we conclude that also in these cases *the dominant contribution to the soft X-ray emission comes from the shocked disk and halo gas rather than from the wind*, just as in the case of model A1.

We can compare the results of our simulations to a simple analytic expression for the approximate X-ray luminosity in the *ROSAT* band (0.1–2.2 keV) of the shocked halo material. We assume spherical symmetry, a uniform halo of constant density n_h, a constant rate of kinetic energy injection by the starburst, and ignore radiative losses from the shocked halo gas (e.g., we assume that the shell's radiative cooling time is

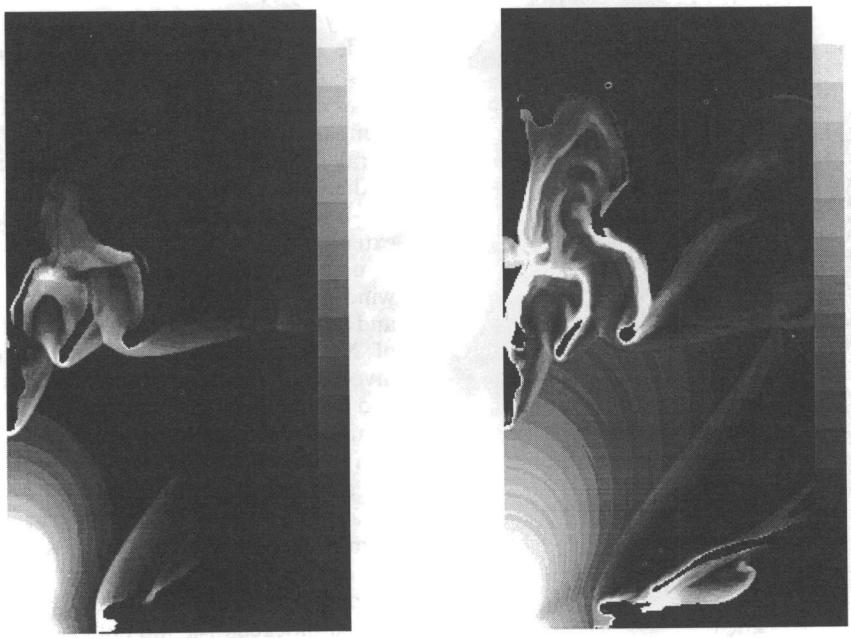

FIG. 22.—Same as in Fig. 4 but for model B2 at 2.0 Myr. The image size is 2 × 4 kpc. The range of log f is [−30.0, −27.0] and [−29.5, −26.5] for the two energy bands, respectively.

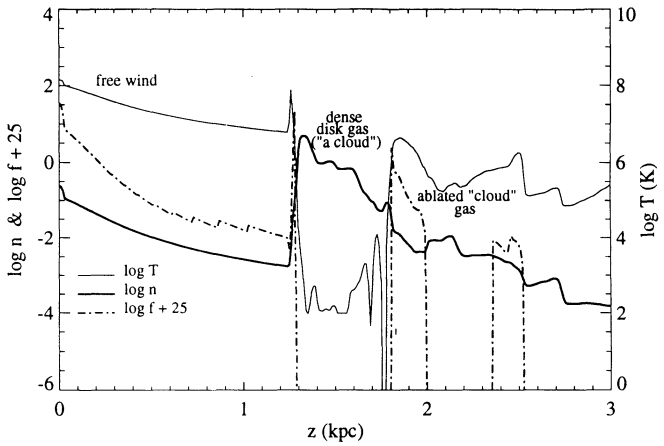

FIG. 23.—Same as in Fig. 5 but for model B2 at 2.0 Myr

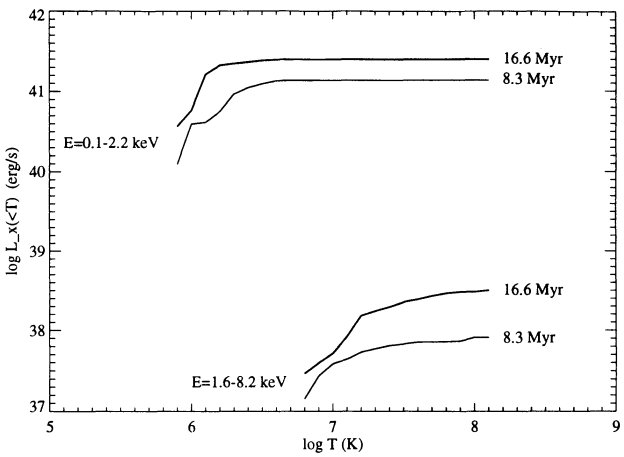

FIG. 24.—Contribution to the X-ray luminosity in the soft- and hard-energy bands from the gas of different temperatures in model A1.

TABLE 2

MASS, X-RAY LUMINOSITY, AND EFFECTIVE TEMPERATURE OF THE X-RAY-EMITTING GAS AT 8.3 Myr IN MODEL A1

Component	log M_{X1} ($M_\odot$)	log L_{X1}[a] (ergs s^{-1})	log L_{X2}[b] (ergs s^{-1})	log L_{Xs}[c] (ergs s^{-1})	log L_{Xh}[d] (ergs s^{-1})	log T_{Xs} (K)
Wind	4.35	37.2	37.2	37.5	37.3	7.5–8.0
Shocked halo	7.35	40.8	39.9	40.8	36.2	6.5
Shocked disk	6.3	40.7	39.5	40.7	37.7	6.35
Total	7.4	41.0	40.1	41.1	37.9	6.45

[a] 0.1–0.7 keV.
[b] 0.7–2.2 keV.
[c] 0.1–2.2 keV.
[d] 1.6–8.3 keV.

NOTE.—In Tables 2–4, log M_{X1} refers to the mass fraction that provides the bulk (>95%) of the total X-ray luminosity in the 0.1–0.7 keV band. Most of the wind X-ray luminosity is due to a very small fraction of the denser wind material while the rest of the wind mass is too tenuous to contribute appreciably to the total wind X-ray emission.

TABLE 3

MASS, X-RAY, LUMINOSITY, EFFECTIVE TEMPERATURE, AND DENSITY OF THE X-RAY–EMITTING GAS AT 16 Myr IN MODELS A1 AND A2

Case	log M_{X1} ($M_\odot$)	log L_{X1}[a] (ergs s^{-1})	log L_{X2}[b] (ergs s^{-1})	log L_{Xs}[c] (ergs s^{-1})	log L_{Xh}[d] (ergs s^{-1})	log T_{Xs} (K)	log n_{X1} (cm^{-3})
A1.....	7.8	41.55	40.4	41.6	38.4	6.4	−1.4
A2.....	7.5	41.8	41.3	41.9	39.5	6.5	−1.1

[a] 0.1–0.7 keV.
[b] 0.7–2.2 keV.
[c] 0.1–2.2 keV.
[d] 1.6–8.3 keV.

NOTE.—In Tables 3 and 4 n_{X1} is the mean density of the gas which provides the bulk of the X-ray luminosity in the 0.1–0.7 keV band. The respective value for model A1 at 8.3 Myr is log $n_{X1} = -1.3$.

TABLE 4

MASS, X-RAY LUMINOSITY, AND EFFECTIVE TEMPERATURE OF THE X-RAY–EMITTING GAS AT 2 Myr IN MODELS B1 AND B2

Case	log M_{X1} ($M_\odot$)	log L_{X1}[a] (ergs s^{-1})	log L_{X2}[b] (ergs s^{-1})	log L_{Xs}[c] (ergs s^{-1})	log L_{Xh}[d] (ergs s^{-1})	log T_{Xs} (K)	log n_{X1} (cm^{-3})
B1.....	6.0	39.8	39.6	40.1	38.5	6.7	−1.1
B2.....	5.1	38.5	37.6	38.6	37.5	6.35	−1.2

[a] 0.1–0.7 keV.
[b] 0.7–2.2 keV.
[c] 0.1–2.2 keV.
[d] 1.6–8.3 keV.

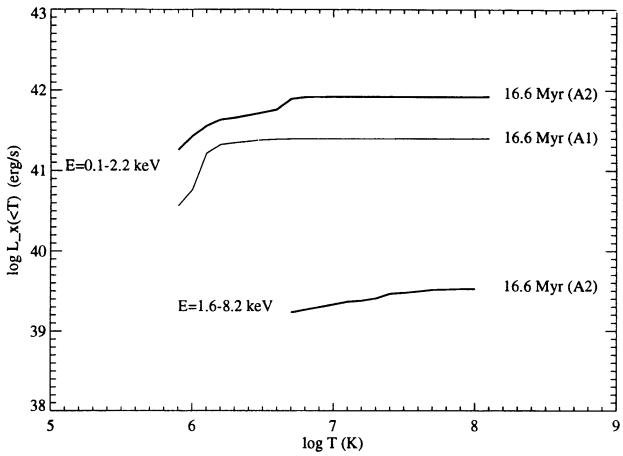

FIG. 25.—Contribution to the total X-ray luminosity in the soft- and hard-energy bands from the gas of different temperatures in Model A2 (*thick lines*). For comparison, the soft X-ray emission for model A1 at 16 Myr, the same as in Fig. 24, is presented (*thin line*).

long compared to its expansion time). We further approximate the shell as having a constant density given by $4n_h$ (strong adiabatic shock), which appears reasonable given the properties of the shocked halo gas in our simulations (see Figs. 5, 11, and 18). We also restrict our treatment to the temperature range for the shocked gas of $\log T = 5.9$–7.3 where the specific emissivity in the *ROSAT* band, Λ_{Xs}, is approximately independent of temperature (see Fig. 1).

Since

$$L_X = \int n^2 \Lambda_x(T) dV \ , \tag{23}$$

the equation (19) of motion for the shell and our simplifying assumptions then imply:

$$L_{X,\mathrm{shell}} = 9.7 \times 10^{40} \dot{E}_{42}^{3/5} n_{h,-2}^{7/5} t_7^{9/5} \ \mathrm{ergs\ s^{-1}} \ , \tag{24}$$

where $L_{X,\mathrm{shell}}$ is the shell X-ray luminosity in the (0.1–2.2) keV band and $n_{h,-2}$ is the halo density in units of 10^{-2} cm^{-3}. We can now compare these predictions to the cases A1 and B1 (in A2 the shell is clearly not adiabatic and in B2 most of the X-rays come from the shocked and ablated disk material). For A1 at 8.3 Myr ($t_7 = 0.83$), we have $\dot{E}_{42} \sim 0.6$, $n_{h,-2} \sim 1.5$, and

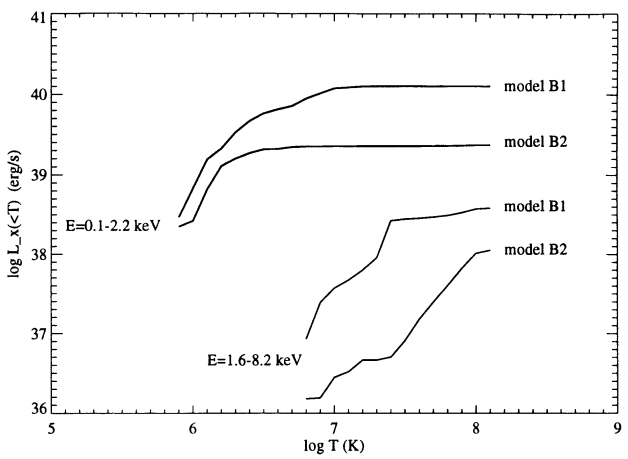

FIG. 26.—Same as in Fig. 24 but for models B1 and B2 at 2 Myr

so we predict $L_{X,\mathrm{shell}} = 7 \times 10^{40}$ ergs s^{-1}, in reasonable agreement with the value derived from the simulation for the shocked gas. At $t_7 = 1.66$ for A1 ($\dot{E}_{42} = 0.9$) we predict $L_{X,\mathrm{shell}} = 3.0 \times 10^{41}$ ergs s^{-1}, compared with $L_{Xs} = 4 \times 10^{41}$ ergs s^{-1} in our simulation. For B1 at $t_7 = 0.2$ we have $\dot{E}_{42} \sim 3$ and $n_{h,-2} \sim 0.8$. Thus, we predict $L_{X,\mathrm{shell}} = 8 \times 10^{39}$ ergs s^{-1}, compared with $L_{Xs} = 1 \times 10^{40}$ ergs s^{-1} in the simulation. In general, we conclude that the simple analytic estimates are in satisfactory agreement with the results of our detailed simulations.

All our models thus show that the wind material itself can account for only a tiny fraction of the soft X-ray flux. If we believe that our models are relevant to the real situation in starbursts, then an immediate prediction is that the *soft X-ray spectra of starburst galaxies need not manifest strongly enhanced heavy element abundance* expected for the material dominated by supernova ejecta.

4.2. *The Nature of the Hard X-Ray-emitting Material*

Inspection of Figures 24, 25, and 26 shows that the hard X-ray emission is dominated by a substantially hotter material as compared to that responsible for the soft emission. The temperature at which the hot gas contributes appreciably to the total hard X-ray flux varies from $\log T \approx 7.3$ for model A1 at 8.3 Myr to $\log T \approx 8.0$ for all other cases considered above, including model A1 at 16.6 Myr. This temperature range is obviously related to the wind material (see Figs. 5, 11, 15, 18, and 23). At the same time there is only very little (if any) hard emission from the gas producing the soft X-ray flux, which is clearly seen from comparing the curves for 0.1–2.2 keV and 1.6–8.3 keV in Figures 24, 25, and 26.

An obvious conclusion emerging from this analysis is that, *unlike the soft emission, a significant fraction of the hard X-ray emission is produced by the wind material.* It is worthwhile emphasizing that this inference applies to all our models despite the dramatic differences between them.

We can compare our simulation results with analytical estimates for X-ray luminosity derived for the case of a spherically symmetric hot wind expanding in ambient gas of a constant density n_h. Equations (7) and (8) in HLA give the following estimates for the temperature and luminosity of the wind material:

$$T_{X,\mathrm{wind}} = 1.7 \times 10^7 (n_{h,-2}^2 \dot{E}_{42}^8 t_7^{-6})^{1/35} \ \mathrm{K} \ , \tag{25}$$

$$L_{X,\mathrm{wind}} = 1.4 \times 10^{38} (n_{h,-2}^{18} \dot{E}_{42}^{37} t_7^{13})^{1/35} \ \mathrm{ergs\ s^{-1}} \ . \tag{26}$$

For the energy injection rate adopted in model B1 and $n_{h,-2} = 0.8$ cm^{-3}, we obtain that, by the time 2 Myr, $\log T = 7.5$ (K) and $\log L_{X,\mathrm{wind}} = 38.4$ (ergs s^{-1}). This agrees well with the temperature range, $\log T_{Xh} = 7.3 - 7.5$, and hard X-ray luminosity, $\log L_{Xh} = 38.5$ (ergs s^{-1}), which our simulations yield for model B1. Similarly, for model B2 at $t = 2$ Myr equations (25) and (26) predict $\log T_{X,\mathrm{wind}} = 7.4$ and $\log L_{X,\mathrm{wind}} = 37.8$ versus the values $\log T_{Xh} = 7.9$ and $\log L_{Xh} = 37.5$ in our simulation (here and below T_{Xh} approximately corresponds to the middle of the temperature range given in Table 5). For model A1 at $t = 8.3$ Myr we predict $\log T_{X,\mathrm{wind}} = 7.2$ and $\log L_{X,\mathrm{wind}} = 37.9$ versus the simulation values of $\log T_{Xh} = 7.0$ and $\log L_{Xh} = 37.7$. At $t = 16.6$ Myr we predict $\log T_{X,\mathrm{wind}} = 7.2$ and $\log L_{X,\mathrm{wind}} = 38.2$ versus the simulation values of $\log T_{Xh} = 7.5$ and $\log L_{Xh} = 38.4$. Note that $\log (L_{Xh}/\dot{E})$ for the gas with $T > 2 \times 10^7$ K ranges from -3.0 to -4.5 for models A1, B1, and B2, which is to be compared to

TABLE 5

TEMPERATURE RANGE IN WHICH X-RAY LUMINOSITY CONTRIBUTION INCREASES FROM 30% TO 90% OF THE TOTAL X-RAY LUMINOSITY IN A GIVEN ENERGY BAND

Model	log T range[a]	T_{Xs}[a,b]	log T range[c]
A1 (8.3 Myr)	6.1–6.45	6.45	6.85–7.1
A1 (16.6 Myr)	6.05–6.4	6.4	7.1–7.8
A2 (16.6 Myr)	6.0–6.7	6.5	<6.8–7.4
B1 (2.0 Myr)	6.3–6.95	6.7	7.3–7.5
B2 (2.0 Myr)	6.15–6.5	6.35	7.8–8.0

[a] 0.1–2.2 keV.

[b] "Empirical" effective temperature, T_{Xs}, is derived from comparing X-ray luminosities in the two "soft" energy bands (see Tables 2–4).

[c] 1.6–8.2 keV.

the value of ≈ -4 predicted by equation (26) for $n_{h,-2} \approx 1$ cm^{-3}. Finally, in model A2 at $t = 16.6$ Myr we predict log $T_{X,\mathrm{wind}} = 7.2$ and log $L_{X,\mathrm{wind}} = 38.3$ versus the values of log $T_{Xh} = 7.0$ and log $L_{Xh} = 39.5$. In this latter case however the hard X-ray emission is apparently dominated by the dense material of the shocked disk and halo gas rather than by the wind. Also equations (25) and (26) are hardly applicable at all in view of an odd morphology of the wind region.

If the hard X-ray emission in starbursts were really dominated by the wind material, we could conclude that the two energy bands considered in this paper would provide an excellent diagnostic for studying two different gaseous species in the region occupied by the wind: the hot ejecta from the starburst region, supposedly enriched with heavy elements, and a much cooler wind-shocked disk and halo gas having a normal chemical composition. However, the observational data does not support the idea that hard X-ray emission represents the thermal emission of the wind plasma. Observations of M82 show that the soft and hard X-luminosities are of the same order of magnitude (see Petre 1993), whereas our models predict hard X-ray luminosity to be 1.3 dex (for model B2) to $\approx$3 dex (models A1 and A2) smaller than soft X-ray luminosity. So we conclude that *the observed hard X-ray luminosity of starbursts is not thermal emission associated with the wind and/or shocked ambient gas* (see also § 4.4 below).

4.3. *Can Gas Clouds Dominate the X-Ray Emission of Starbursts?*

As mentioned in the preceding section, model B2 provides an idea of what the effects of gas clouds interacting with the wind may be. The model allows us to suggest that most of the thermal X-ray emission of starburst galaxies, including "mature" starbursts, may be due to gas clouds that get into the region occupied by the wind and get shocked and ablated by the latter. The soft X-ray emitting material in model B2 has a very high density, $n \sim 10^{-1}$ cm^{-3}, which is about two orders off magnitude higher than the initial density of the halo gas, and this material is certainly related to the dense cometary blobs seen in Figures 21 and 22. As the simulation results show, even a very small mass of such a dense gas in the halo of the galaxy, $M \sim 10^5\ M_\odot$, is capable of producing a significant soft X-ray flux. In general, even after the superbubble is formed, the host galaxy for the starburst could keep sending in clouds into the outflowing wind region, which would enhance the soft X-ray luminosity for a given strength of central starburst activity. In view of the fact that starbursts have, as a rule, a rich and highly disturbed gaseous component, it does not seem to be a problem to feed the neighborhood of the starburst region and the halo of the galaxy with gas clouds in amounts sufficient to keep the mass of X-ray–emitting material on the level a couple of magnitude higher than that in model B2, which would provide X-ray luminosity typical for starbursts similar to M82. In this respect, it is suggestive that, on the one hand, a tiny central region of M82, $r \sim 350$ pc, contains a huge mass of dense molecular clouds ($M \sim 10^8\ M_\odot$; e.g., Turner, Martin, & Ho 1990). On the other hand, the gas in this region exhibits features of inflow, with gas velocities of $\sim$50 km s^{-1} (e.g., Seaquist, Bell, & Bignell 1985). This seems to indicate that there is enough inflowing gaseous material which is capable in principle of feeding the region of the wind-cloud interaction.

It is also worthwhile noting that in a real three-dimensional situation the hydrodynamical disruption and ablation of clouds proceeds much more efficiently than in the two-dimensional case considered in this paper (e.g., Stone & Norman 1992). So, conversion of dense cold material into X-ray–emitting gas should be more efficient than implied by the results from model B2.

Thus we may easily envision a scenario in which clouds are continuously supplied to the wind region of the starburst galaxy and are then shocked, accelerated, and ablated by the wind, providing material for the major soft X-ray emission of the starbursts.

4.4. *The Temperature of the X-Ray-emitting Gas*

Thermal X-ray emission in different energy bands may arise in different gaseous constituents having very different temperatures, densities, etc. Therefore multiband data may provide a valuable tool to study the complex "anatomy" of the superwind region. Important information about the nature and state of the X-ray emitting gas can be drawn from comparing luminosities in the energy bands isolated above. To illustrate this, consider first the two adjacent bands constituting our soft band 0.1–2.2 keV. For model B2 at 2 Myr we have log L_{X1} − log $L_{X2} = 0.7$. Under the adopted specific emissivities (Fig. 1) this difference implies the "effective" temperature of the X-ray emitting gas $T_{Xs} \approx 3 \times 10^6$ K. Similarly, the effective temperature for the model B1 turns out to be $T_{Xs} \approx 5 \times 10^6$ K. These temperature estimates are given in Table 4. They can be interpreted as typical values for the bulk of the X-ray–emitting gas whose actual temperatures range basically within 10^6–10^7 K. As seen from Figure 1, if the prevailing temperatures were larger than $\sim 6 \times 10^6$ K, we should expect the 0.7–2.2 keV luminosity to dominate over that in the 0.1–0.7 keV band, which is not the case for the model situations under discussion. On the other hand, if most of the X-ray–emitting gas had temperatures below $\sim 2 \times 10^6$ K, the ratio L_{X2}/L_{X1} would be much smaller than that in Table 4. Comparison of the values for T_{Xs} in Table 4 with the hydrodynamical temperatures in Figures 18–23 at which the soft X-ray emissivity is sufficiently large reveals a good degree of consistency between T and T_{Xs}. Similar estimates for the effective temperature in models A1 and A2 are given in Tables 2 and 3. Again, the derived temperature values turn out to be quite consistent with the temperatures in Figures 5, 11, and 15.[3]

[3] It should be emphasized that there is a larger uncertainty in deriving the effective X-ray temperature for the wind material as compared to the case of the disk and halo gas. The dependence of log L_{X2} − log L_{X1} on T_{Xs} above $T_{Xs} \approx 3 \times 10^7$ K is so weak as to allow, within the range of uncertainties, the temperature to be placed essentially anywhere between $T \approx 6 \times 10^6$ and $T \approx 1 \times 10^8$ K. Inspection of Fig. 5 definitely favors high temperatures; therefore in Table 2 we give the upper end of the "allowable" temperature range.

We can also compare the above "empirical" values of the effective temperature (i.e., the ones which can be obtained from observed X-ray luminosities) with the "theoretical" effective temperatures derived from the curves $L_X(<T)$. Figures 24–26 and the data in Table 5 show that both temperatures excellently agree with each other. Therefore, in general, we conclude that *X-ray measurements in the bands close to the ones which we have isolated for our analysis*, 0.1–0.7 keV *and* 0.7–2.2 keV, *can really provide a good diagnostic for the temperature of the soft X-ray emitting gas.*

Comparing the values of T_{Xs} for models A1, B1, and B2, we observe that, despite very large differences both in gaseous constituents and mass and energy injection rates, all models yield very similar effective temperatures for the soft X-ray emitting material, $T_{Xs} = 2\text{–}5 \times 10^6$ K. Comparison of the effective temperature values in model A1 at two very different epochs additionally reveals a remarkable persistency of this parameter. To some extent this is due to a dramatic drop of the X-ray emissivity in 0.1–2.2 keV band below log $T = 6.0$. However, within the temperature range log $T = 6.0$–7.0 this emissivity remains essentially constant, so the effective upper limit of log $T \approx 6.5$ is associated with a real deficiency of sufficiently dense gas at these temperatures. Anyway, our results encourage us to predict that *the bulk of starbursts should have effective temperatures of the soft X-ray emitting gas close to* $T_{Xs} = 2\text{–}5 \times 10^6$ K provided their X-ray emission is the thermal emission of a hot gas with chemical composition not very much different from solar.

As seen from Figures 24–26 and Table 5, the temperatures of the hard X-ray–emitting gas are substantially higher. If there is a hard thermal X-ray emission coming out from the starburst cloudy halos, we would predict that the corresponding temperatures should be of the order of 10^8 K.

We can compare our predictions with recent results provided by *ROSAT* and BBXRT. As emphasized by Petre (1993), the fundamental new result from these X-ray observations obtained for M82 and NGC 253 is that the "hot" X-ray emission corresponding to temperatures $\sim 8 \times 10^7$ K arises only in the bulge region while the emission of the extended X-ray halo corresponds to much lower temperatures of several 10^6 K. So, the inferred temperatures of the extended X-ray halos of these galaxies are quite compatible with the predicted values for the soft X-ray emission.

As regards the hard component, both the required temperatures and spatial distribution may also be represented by our models. The predicted hard X-ray emission is much more centrally condensed than soft emission, and the predicted temperature range, log $T_{Xh} = 7.0$–8.0, is consistent with the estimate log $T_X = 7.8$ derived by Ohashi & Tsuru (see Petre 1993) for M82. However, a very low ratio of hard-to-soft X-ray luminosities yielded by our models, on one hand, and the absence of the 6.7 keV Fe K line which should be present in the emission of a hot gas, from the other hand, makes the latter a poor candidate for the starburst hard–X-ray emitter. The data are consistent with a hot X-ray emitting gas if the gas metal abundance is below 0.3 solar. But the low value of L_{Xh}/L_{Xs} predicted by our models makes this option unlikely either. It is worthwhile noting here that high-mass X-ray binaries have spectra hotter than 10^8 K and are thus excluded as a source of hard X-ray emission by the spectra provided by *Ginga* and BBXRT; on the other hand, low-mass X-ray binaries can hardly be associated with starburst regions (see Petre 1993). Another candidate for producing hard X-ray emission might be the inverse compton scattering of infrared photons. However, as stated by Petre (1993), the hard X-ray continuum is definitely not of power-law form as would be expected in this case.

4.5. *Relation to Optical Line-emitting Gas*

As the hot gas in the starbursts center expands and drives into the main body of the disk, the dense disk gas is being dragged into the halo where it forms the walls of the biconic cavity and produces extended dense "filaments." The gas is expected to be shock-ionized and also photoionized by the UV-radiation which freely escapes from the starburst region along the cavity axis. This makes the pushed-up disk gas an excellent candidate for optical line-emitting filaments observed in starbursts (see examples as well as relevant discussion in HLA). The morphology of the density distribution in Figures 6 and 12 as well as the velocity of the dense material in Figure 8 are definitely very suggestive of streaks of ionized gas protruding out from the central regions of starbursts with typical velocities of a few hundred km s^{-1} inferred for this gas (e.g., HAM).

The "comets" seen in Figure 21 give an idea of how line-emitting filaments can arise as the wind interacts with gas clouds in the galaxy halo. Depending on the initial location and velocity of the clouds, these filaments may also reside within the cavity.

Finally, Figure 16, which exhibits a spectacular bright thin shell developed in model B1, provides an example of how very extended Hα arcs of the kind observed in Arp 220 can arise. The line-emitting gas morphology in Arp 220 strongly resembles the shell in Figure 16 and is suggestive of a galactic superwind which has not reached as yet the "blow-out" phase. It should be remembered, of course, that the observed Hα image of Arp 220 represents the *surface* brightness distribution, i.e., the integral of the Hα emissivity along the line of sight, while Figure 16 gives the *cross-sectional* view of the density and temperature. Analysis of model B1 suggests that, to produce arcs similar to those in Arp 220, the preburst galaxy should posses a substantial amount of dense gas in the nearest vicinity of the starburst region, and it should also contain an appreciable halo component. The nearby dense gas should be responsible for the luminous material itself, whereas the halo gas should provide confinement to the wind and dense bubble's shell and prevent the disruption of the latter.

4.6. *Morphology of the Wind Region*

The hot gas supplied by exploding supernovae and stellar winds sweeps out the disk gas above the starburst region and drives shocks propagating in the disk and the halo. Eventually it blows out a biconic cavity which collimates the outflowing wind material, channeling it up into the halo. Its shape depends on the rate of the energy release in the center of the galaxy as well as on the density and scale height of the gas within the disk which has to provide confinement to the hot gas within the cavity.

As argued in § 1, the starburst galaxies do show distinct features of a biconic geometry suggestive of a corresponding cavity through which the hot central gas is emanating. So the above scenario for the formation of biconic cavities seems to be quite a natural explanation for the origin of these features. The challenge, however, is to understand how the observed shape and size of the cavities can be made compatible with the observed mass and energy injection rates and with the mass and structure of the confining gas.

In model A1, the cavity collimating "nozzle" has a radius of

$\sim$300 pc by the time 8.3 Myr, its opening angle being $\sim 70°$ (see Fig. 3), while the height of the region occupied by the wind material is 3.2 kpc. This makes the ratio of the wind region height to the radius of the "nozzle" $a = z_w/r_n \approx 10.5$. In model B1, however, the nozzle radius is already twice as large by the time 2 Myr, although the vertical extension of the wind material is ~ 1 kpc smaller than in A1; the corresponding value of a is $a \approx 3.5$. Since the gaseous disk and halo components in both models are essentially the same, we conclude that the history of energy deposition plays a crucial role in shaping the collimating nozzle. In model A1 the energy ejection rate is initially about two orders of magnitude lower than in B1, and it increases gradually by an order of magnitude by the time 8.3 Myr (see Fig. 10 in Leitherer et al. 1992). The much milder energy release inflicts much less damage to the gas in the plane of the disk, while still allowing the wind to break through vertically. The result is that at the later, much more violent phases of the starburst there is a ready way for the energy to escape freely from the site where it is released, without strongly affecting the gaseous disk.

Model B2, which has a very feeble halo and whose disk has a smaller scale height than that of B1, seems to manifest the collimating effect to a much less degree. Yet a closer inspection reveals a bipolar geometry and features of biconic cavity. The ratio of the free wind vertical extension to the wind radial extension at the base of the disk is $a \sim 3$, and the opening angle of the cone that confines the free wind region by extended oblique shocks is $\sim 90°$.

A general conclusion to be made from our models is that starbursts with very different structures in their gaseous components and having very different mass and energy injection rates may easily develop bipolar winds without any preexisting collimating funnels.

5. CONCLUSIONS

In this paper we have conducted hydrodynamical simulations of galactic superwinds for different models of a starburst galaxy. We have analyzed the interaction of the galactic wind with the ambient interstellar medium that has a two-component disk-halo structure. The simulation results have shown the following.

1. Clear-cut bipolar winds develop in model galaxies without a preexisting collimating funnel in the galaxy gaseous component, and a biconic cavity confned by dense shocked disk material arises easily under very different conditions.

2. A tenuous halo leads to a much better conformity of the wind region geometry with the observed starburst X-ray morphology than the case of an unrealistically high gas density in the galaxy halo (implied, e.g., by the model of TI).

3. Unlike the well-studied case of a hot bubble expanding within a one-component ambient gas, the interior of the wind–blown-out bubble in our two-component models eventually gets filled with dense "filaments" of the wind-entrained disk material. Also the gas kinematics differs substantially from that derived for "ordinary" hot bubbles. The velocity pattern is dominated initially by the central biconic outflow, with large-scale vortices becoming, however, increasingly dominant as the wind becomes "mature."

4. The history of mass and energy deposition in the starburst region of the galaxy is crucial for the wind development. A "milder" early wind, which is associated with the initial mass and energy deposition due to stellar winds of massive stars, produces a bipolar vertical cavity in the disk and halo gas without strongly affecting the gaseous disk and thus creates conditions for the virtually free vertical escape of the hot gas at the later, much more vigorous supernova-dominated phases of the starburst.

We have calculated the X-ray emission in three energy bands, as well as the mass and effective temperature of the X-ray–emitting gas, and estimated the contribution of different gaseous components to the integrated X-ray flux. Also we have briefly analyzed the dense gas filamentary structure exhibited by our models and concluded that it may be pertinent to the optical-line emission of starbursts. The inferences and predictions that we have made in regard to X-ray and optical-line emission can briefly be summarized as follows.

1. The observed soft X-ray luminosity of starbursts can be accounted for by the emission of the wind-shocked disk and halo gas, so there is no urgent need to invoke nonthermal emission mechanisms (like Compton scattering of infrared photons on relativistic electrons).

2. The bulk of thermal soft X-ray emission from starbursts should be due to the shocked disk and halo material rather than to the wind material. A preliminary conclusion is made that dominant contribution to this emission may come from gas clouds which are shocked and ablated by the wind.

3. The simulation results allows us to predict that *temperatures of the extranuclear soft X-ray emitting gas in starburst galaxies should be close to* $T_{Xs} = 2$–5×10^6 K. We have found that typical temperatures of the bulk of the soft X-ray-emitting material in our very different models agree very well with the ones estimated on the basis of *ROSAT* data.

4. We predict that *soft X-ray spectra of starbursts need not show any significant overabundance of heavy elements.*

5. Unlike soft X-ray emission, the hard component of the thermal X-ray emission is found to be dominated by wind material. The luminosity of this component turns out to be much less than is observed, and we predict that *the observed hard X-ray emission of starbursts is associated with neither thermal wind fluid nor shocked ambient gas.*

6. Optical emission-line clouds are most likely to be disk material that has been entrained by the wind and propelled into the galaxy halo.

We acknowledge the support of NASA grants NAGW-3138, NAG 5-1368, and NAG 5-1785 for the research reported here. A. S. also thanks the STScI Visitor Program for financial support during the early stages of this project. D. B. thanks J. Krolik for support and encouragement in doing this work. Support of NASA grant NAGW-2012 is also acknowledged, as is supercomputing support from SDSC.

REFERENCES

Arthur, S. J., Dyson, J. E., & Hartquist, T. W. 1993, MNRAS, 261, 425
Balsara, D. S. 1994a, ApJ, 420, 197
———. 1994b, in preparation
Berman, V. G., & Suchkov, A. A. 1991, Ap&SS, 184, 169
Bernlöhr, K. 1993, A&A, 268, 25
Burbidge, E. M., Burbidge, G. R., & Rubin, V. C. 1964, ApJ, 140, 942
Collela, P., & Woodward, P. R. 1984, J. Comput. Phys., 54, 174
Cowie, L. L., McKee, C. F., & Ostriker, J. P. 1984, ApJ, 247, 908
Danly, L., Lockman, F. J., Meade, M. R., & Savage, B. D. 1992, ApJS, 81, 125
Dyson, J. E. 1993, in IAU Symp. 155, Planetary Nebulae, ed. R. Weinberger & A. Acker (Dordrecht: Kluwer)
Fabbiano, G. 1988, ApJ, 330, 672

Fabbiano, G., Heckman, T. M., & Keel, W. C. 1990, ApJ, 355, 442
Hartquist, T. W., & Dyson, J. E. 1993, QJRAS, 34, 57
Heckman, T. M., Armus, L., & Miley, G. K. 1987, AJ, 93, 276
———. 1990, ApJS, 74, 833 (HAM)
Heckman, T. M., & Fabbiano, G. 1994, in preparation
Heckman, T. M., Lehnert, M. D., & Armus, L. 1993, in Proc. of Evolution of Galaxies and Their Environments, in press (HLA)
Koo, B.-C., & McKee, C. F. 1992, ApJ, 388, 93
Landau, L. D., & Lifshitz, E. M. 1987, Course in Theoretical Physics, Vol. 6 (2d ed.; Oxford: Pergamon)
Leitherer, C., Robert, C., & Drissen, L. 1992, ApJ, 401, 596 (LRD)
Mathews, W. G., & Doane, J. S. 1994, Lick Obs. Bull., in press
McKee, C. F., Van Buren, D., & Lazareff, B. 1984, ApJ, 278, L118
Nakai, N., Hayashi, M., Handa, T., Sofue, Y., Hasegawa, T., & Sasaki, M. 1987, PASJ, 39, 685
Petre, R. 1993, in The Nearest Active Galaxies, ed. J. Beckman, L. Colina, & H. Netzer (Madrid: Consejo Superior de Investigaciones Cientificas), 117
Pietsch, P. 1993, in Physics of Nearby Galaxies: Nature or Nurture?, ed. T. X. Thuan, C. Balkowski, & J. T. T. Van (Paris: Editions Frontiers), p. 67
Raymond, J. C., Cox, D. P., & Smith, B. W. 1976, ApJ, 204, 290
Seaquist, E. R., Bell, M. N., & Bignell, R. C. 1985, ApJ, 294, 546
Stone, J. M., & Norman, M. L. 1992, ApJ, 390, L17
Tomisaka, K., & Bregman, J. N. 1993, PASJ, 45, 513
Tomisaka, K., & Ikeuchi, S. 1988, ApJ, 330, 695
Turner, J. L., Martin, R. N., & Ho, P. T. P. 1990, ApJ, 351, 418